Electronic Supplementary Material (ESI) for Energy & Environmental Science.
This journal is © The Royal Society of Chemistry 2022

Supplementary Information

Bisulfate Transport in Hydrogels for Self-healable and Transparent Thermoelectric Harvesting Film

Cheolhyun Cho, Byeonggwan Kim,* Sienoh Park and Eunkyoung Kim*

Department of Chemical and Biomolecular Engineering, Yonsei University, 50 Yonsei-ro, Seodaemun-gu, Seoul 03722, South Korea

E-mail: *Prof. E. Kim, eunkim@yonsei.kr, *Dr. B. Kim, loveichem2@yonsei.ac.kr

Contents

1. Experimental Section

Materials

Poly(2-acrylamido-2-methyl-1-propanesulfonic acid) solution (PAMPS, weight average molecular weight = 2,000,000, 15 wt% in water), poly(vinyl alcohol) (PVA, weight average molecular weight = 89,000-98,000, 99+% hydrolyzed), ammonium persulfate (APS), salicylaldehyde, 7-amino-4-(trifluoromethyl) coumarin, and tetra-n-butylammonium bisulfate ([TBA][HSO_4]) were purchased from Sigma Aldrich. 3,4-Ethylenedioxythiophene (EDOT) was purchased from TCI Co., Ltd. Deionized (DI) water (Extra Pure) was purchased from Duksan General Science. Cerasolzer #186 (indium wire) was purchased from Kuroda Electric Co. LTD. The chemicals were used in the experiment without further treatment.

Synthesis of NPP solution

A PAMPS solution (15 wt% in water) was diluted to 4.9 wt% using DI water. PVA was added to the PAMPS solution (0, 2, 9, or 16 wt% PAMPS), and the mixture was stirred at 80°C for 3 h. After the PVA was fully dissolved, the solution was cooled to room temperature, and EDOT was added to the solution at a specific concentration. Subsequently, 1 molar equivalent APS (0.7 M solution)[1, 2] in EDOT was added to the solution as an oxidizing agent, and the solution was stirred at room temperature for 72 h to synthesize the PVA/PEDOT/PAMPS composite. To increase the bisulfate concentration in solution, additional APS (1, 2, 3, or 4 molar equivalent EDOT) was added to the PVA/PEDOT/PAMPS solution and stirred at room temperature for 3 h. Next, the solution was washed with diethyl ether to remove unreacted EDOT monomer and oligomers to obtain a blue solution. The EDOT concentrations of the solutions were 0.33, 0.52, 0.65, 0.78, 0.97, and 1.3 wt% in solid contents, and the corresponding samples were named NPP33, NPP52, NPP65, NPP78, NPP97, and NPP130, respectively.

Film fabrication

Two of Au electrode lines (thickness: 100 nm, width: 1 mm, length: 2 cm, and distance between electrodes: 3 mm) were deposited on top of a clean polyethylene terephthalate film (PET, thickness: 0.5 mm) by thermal evaporation under a high vacuum (5×10^{-6} Pa) through a stainless steel shadow mask. The Au-deposited PET film was cut to a size of 0.5×3 cm^2, and an area of 0.5×0.5 cm^2 was treated with O_3 plasma for 5 min. The NPP solution (30 μL) was drop-casted on the O_3 plasma-treated active area and dried at room temperature and 50% relative humidity (RH) for 3 h. Subsequently, the dried film was stored in a chamber at 80% RH.

The thickness of the NPP films was measured using a surface profiler at various RH levels (Figure S3). Because the NPP film was formed by drop-casting on the O_3 plasma-treated PET surface and subsequent drying, it formed a flat film on the PET surface with the control of the solution volume and drop-casted area. Above 70% RH, owing to the swollen films, the film became soft, but the thickness of the film was measurable using stylus force because the surface was not indented from the scanning process. The NPP films were uniformly coated with a thickness of 60 μm and 80% RH. The film thickness was equal to 60 μm within the experimental error for all samples prepared for further characterization and measurement of the TE properties.

Fabrication of iTE modules

A PET film (thickness: 0.5 mm) with 20 legs of the Au electrode (thickness: 100 nm, width: 2 mm, and distance between electrodes: 5 mm) was prepared using the same process as described above. An area of 2×7 mm^2 was treated with O_3 plasma for 5 min. The NPP65-3 solution (10 μL) was drop-casted on each leg and dried at room temperature for 1 h. The dried module was stored in a chamber at 80% RH. For the wearable module device, a 30 nm–thick Au electrode was deposited on a 60 μm–thick PET film, and the dyed NPP65-3 solution (10 μL) was dropped onto an active area of 2×5 mm^2. Subsequently, it was dried at room temperature for 1 h. Commercial water-soluble inks with red, yellow, and blue color for inkjet printers (1 mL) were mixed with 2 mL of the NPP65-3 solution to

obtain the dyed NPP65-3 solution. Orange, green, and purple inks were prepared by mixing two of the three inks in a 1:1 volume ratio.

Screen printing of colored iTE modules

Dyed NPP solution (0.3 mL) was dried on a glass slide (2.5 × 2.5 cm^2) for 3 h at room temperature. The prepared paste was inked on a blade and was slid on a stainless-steel pattern mask with a hole measuring 2 × 6 mm^2, which was placed on an Au-patterned PET film. The patterned paste was dried for 3 h at room temperature, following which the wearable module was worn on a human wrist to measure the ionic thermal voltage.

Synthesis of (7*E*)-7-(2-hydroxybenzylideneamino)-4-(trifluoromethyl)-2*H*-chromen-2-one (BDC)

The bisulfate detecting coumarin (BDC) was synthesized by the procedure described in the literature.[3] Briefly, salicylaldehyde (0.29 g, 2.18 mmol), 7-amino-4-(trifluoromethyl) coumarin (0.5 g, 2.18 mmol), and absolute ethanol (30 mL) were added to a 100 mL two-neck round bottom flask. The reaction mixture was refluxed for 2 h, then it was cooled down to room temperature to give the orange solid (0.57 g, 1.2 mmol) in 78% yield. ^{1}H NMR (CD_3CN, 300 MHz) δ 12.71 (s, 1H), 8.88 (s, 1H), 7.82 (q, J= 8.7 Hz, 1H), 7.59-7.57 (m, 1H), 7.50-7.40 (m, 3H), 7.04-6.99 (m, 2H), 6.85 (s, 1H).

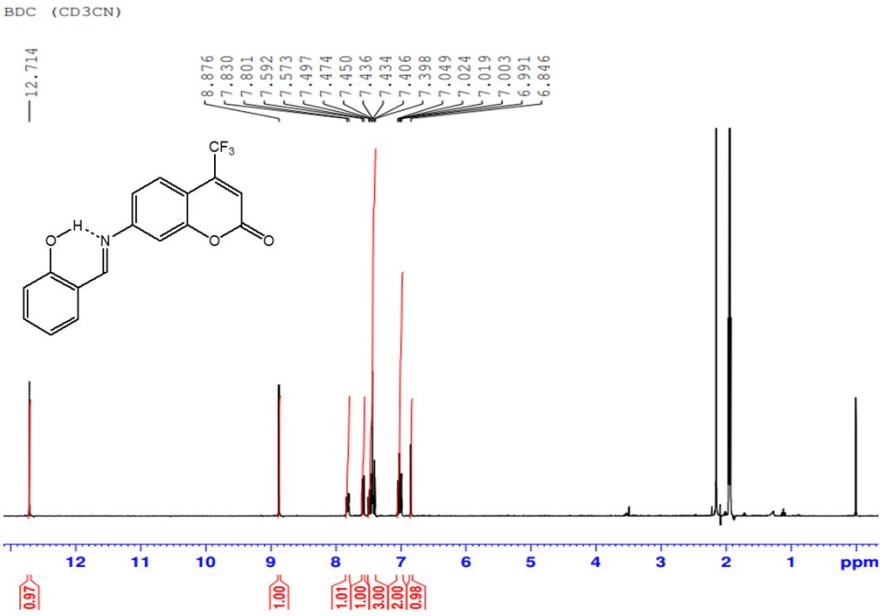

^{1}H NMR spectrum of BDC in CD_3CN.

Fluorescence titration

BDC was dissolved in a CH_3CN:H_2O (1:1 v/v) solvent to a concentration of 3 μM, as reported in the literature.[3, 4] To obtain a standard titration curve, [TBA][HSO_4] was dissolved in the prepared BDC solution to obtain 0–7 molar equivalent BDC, and the fluorescence spectra of the solutions were obtained at an excitation wavelength of 370 nm (Figure 2d, dashed line). Subsequently, the maximum peak intensity at 485 nm was linearly fitted to the [TBA][HSO_4] concentration to obtain the standard fit values (Figure S6c). The maximum peak intensities were nearly proportional to the [TBA][HSO_4] concentration in this concentration range. The NPP65 solution with various APS contents was diluted to 3 μM BDC solution at a volume ratio (V_{NPP65}/V_{BDC}) of 1/300. A negligible effect was observed in the fluorescence spectrum when the very light blue color of the NPP65 solution was diluted in the BDC solution, which was confirmed by adding the same concentration of PEDOT:PSS solution to the BDC solution.

^{1}H NMR spectroscopy and pulsed-field-gradient NMR diffusometry.

Solid-state ^{1}H NMR spectra were obtained using a Bruker Avance III HD 500 MHz (11.7 T) spectrometer equipped with a diff30 pulsed-field-gradient diffusion probe (National Center for Inter-University Research Facilities, Seoul National University). The pulsed-field-gradient spin-echo sequence for all samples was set as 9.8 μs for 90° radio frequency (RF) pulses with a gradient pulse duration (δ) of 1.0 ms, diffusion times (Δ) of 50.0 ms, and gradient strength of 100%. A single 90° RF pulse with a 9.8 μs duration at 29 W was used, and the ^{1}H NMR spectra were collected at an acquisition time of 1.0922667 s, prescan delay of 6.5 μs, and relaxation delay of 4.0 s. The spectra were obtained from 16 scans for each condition. Five temperature steps from 25 °C to 45 °C in 5 K intervals were used. The NPP65-1 and NPP65-3 solutions (20 mL) were dried on a Teflon mold (5 × 5 × 0.5 cm^3) for 72 h at room temperature to obtaining flexible films, which were kept in 90% RH for 24 h at room temperature for moisturizing. Subsequently, the films (mass: 225 mg) containing additional moisture (mass: 22.5 mg) were filled in a 5 mm NMR tube to a length of 4 cm to fill the coil region of the probe.

The diffusion coefficient of protons (D_{H^+}) of the films at various temperatures was determined using the Stejskal–Tanner equation:[5]

$$I_g = I_{g=0} e^{-D\gamma^2 g^2 \delta^2 (\Delta - \delta/3)} \quad \text{(Equation S1)}$$

where I_g is the signal intensity at a gradient strength (g), g is the gradient strength, D is the diffusion coefficient of nuclides, γ is the gyromagnetic ratio (26752 rad s^{-1} G^{-1} for ^{1}H), δ is the gradient pulse duration, and Δ is the diffusion time.

The activation energies (E_a) of the films were determined using the Arrhenius equation:

$$D = D_0 e^{-E_a/kT} \quad \text{(Equation S2)}$$

where D_0 is the diffusion at infinite temperature, k is the Boltzmann constant, and T is the absolute temperature.

Figure S9a,b shows ^{1}H spectra for NPP65-1 and NPP65-3 films at different temperatures. A broad peak at 7.55 ppm was obtained for NPP65-1 at 25 °C, which was gradually shielded to 7.44 ppm

as the temperature was increased to 45 °C. However, NPP65-3 showed broad peaks at 7.95, 8.41, and 9.59 ppm, which were similarly shielded (~0.2 ppm) as the temperature was increased. This small shielding effect with increasing temperature may be attributed to a small water loss from the hydrogel matrix.[6] The resonance and shielding of sulfonic acid in the solid-state NMR spectra are consistently larger than those of free protons in the solution NMR spectra.[7] Additionally, the full width at half maximum (FWHM) for NPP65-3 (700 Hz) at 25 °C is higher than that for NPP65-1 (270 Hz), implying that the former has 2.6 times faster spin–spin relaxation (T_2) and thereby indicating the slower motion of protons (slower proton exchange).[7] The D_{H^+} of NPP65-1 (1.24×10^{-9} m^2 s^{-1}) was larger than that of NPP65-3 (1.17×10^{-9} m^2 s^{-1}) at 25 °C (Figure S9c), and these values were similar to the D_{H^+} of Nafion with high water uptake (~1×10^{-9} m^2 s^{-1}).[6] In addition, the D_{H^+} of both films at 50% RH was difficult to measure, which may explain a small iTE effect at low humidity resulting from a small ion channel and strongly bonded ions in the hydrogel matrix.

Raman spectroscopy

PAMPS showed strong characteristic peaks at 1042 and 771 cm^{-1}, assigned to the symmetric stretching vibration of deprotonated SO_3^- and the N–H stretching band, respectively.[8, 9] For NPP65-1, the most intense peak was found at 1438 cm^{-1}, which could be attributed to the symmetric stretching mode of C_α=C_β in PEDOT.[10, 11] The bands at 1567 cm^{-1} and 1499 cm^{-1} were assigned to the asymmetric C_α=C_β stretching vibration of the thiophene ring, and the band at 1535 cm^{-1} originated from the splitting of the asymmetric C_α=C_β stretching vibration.[12] Furthermore, a SO_2 bending band was found at 441 cm^{-1}.[13] For NPP65-2 and NPP65-3, which had higher APS contents, the symmetric stretching mode of C_α=C_β at 1438 cm^{-1} was blue-shifted to 1441 and 1442 cm^{-1}, respectively, which was associated with an increase in doping level by sulfate and bisulfate anions.[13-15] In the case of NPP65-4 and NPP65-5, it was further blue-shifted, but the peak intensity was decreased, which may be attributed to the

decomposition of the PEDOT induced by the presence of high APS contents.[2] With increasing APS content, the bands related to the asymmetric C_α=C_β stretching vibration were shifted from 1499 cm^{-1} to 1508 cm^{-1} by the increase in the bisulfate anion content, which agrees with a previous report.[13] In addition, the SO_2 bending band of the sulfonates was shifted from 441 to 444 cm^{-1} with increasing APS content, leading to increased doping by the bisulfate anion.

X-ray photoelectron spectroscopy

The deprotonation of PAMPS was also determined by X-ray photoelectron spectroscopy (XPS) analysis, which was conducted for PAMPS and NPP65-3 with different PVA contents in wt% (Figure S7). The S 2p spectra were deconvoluted into four peaks, which included deprotonated the -SO_3^- (167.6 and 168.7 eV) of PAMP–SO_3^- and protonated -SO_3H (168.5 and 169.9 eV) of PAMP–SO_3H with two spin orbit peaks ($2p_{1/2}$ and $2p_{3/2}$, respectively).[16, 17] With increasing PVA content, the -SO_3^- content increased from 48% to 52% and 58% for 0, 2, and 16 wt% of PVA in NPP65-3, respectively. The increase in -SO_3^- content could be attributed to the increased dissociation of -SO_3H in PAMPS. The dissociation of -SO_3H by XPS analysis was in good agreement with the increase in $\boldsymbol{RI_{1040}}$ by Raman analysis, as mentioned above.

Bisulfate generation

$$S_2O_8^{2-} + H_3O^+ \rightarrow HSO_8^- + H_2O \rightarrow HSO_4^- + HSO_5 \quad \text{(Acidic solution)} \quad \text{(Equation S3)}$$

$$HSO_5 + H_2O \rightarrow H_2SO_4 + 1/2O_2 + H_2O \quad \text{(Acidic solution)} \quad \text{(Equation S4)}$$

$$H_2SO_4 + H_2O \rightleftharpoons HSO_4^- + H_3O^+ \quad \text{(Acidic solution)} \quad \text{(Equation S5)}$$

$$S_2O_8^{2-} + H_2O \rightarrow 2HSO_4^- + 1/2O_2 \quad \text{(Neutral solution)} \quad \text{(Equation S6)}$$

In Equation (S3−S6), persulfate reacts with protons to produce bisulfate at a moderate temperature of 25 °C and an acidic (or a neutral) condition.[18, 19]

Characterization

The thickness of the films was measured by a Bruker Surface Profiler (DektakXT). The films were stored in the chamber with corresponding RH level, taken out immediately prior to measurement, and the line profile was measured within 30 s. The active area (5 × 5 mm^2) and thickness (60 μm) of the films were the same for all film sample used for measuring thermoelectric properties.

UV-vis-NIR spectra of the NPP films (thickness of 60 μm) were measured by Lambda 750, UV/Vis/NIR Spectrophotometer, PerkinElmer.

Fluorescence spectra were obtained by a luminescence spectrometer (Perkin Elmer, Model LS55). For fluorescence switching in Figure 2e-h, the NPP65-3 film was prepared on PET (area=1×2 cm^2) by dropcast 240 μL of NPP65-3 solutions and dried for 3 h at RT. Then, 100 μL of dimethylformamide was dropcast on the film for visualize fluorescence property of BDC by wetting. A temperature gradient (ΔT) cycles of 22 K by applying a current of 1.1 A to a Peltier module bottom of the film were repeated for 60 s on the both parts of the film. The fluorescence intensity change was monitored under a hand-held UV lamp (~365 nm) and simultaneously temperature of the film was measured by a high-resolution IR camera (FLIR E40). The photo images with fluorescent light was processed with ImageJ software.

The 300 MHz ^{1}H-NMR spectrum was obtained using a Bruker biospin AVANCE III HD 300 spectrometer with CD_3CN and tetramethylsilane as the solvent and internal reference, respectively.

Transmission electron microscopy (TEM) image and electron diffraction pattern were obtained by JEM-F200, JEOL Korea Ltd. Diluted (1/100) NPP65-3 solution of 5 μL was dropcasted on a carbon film-coated TEM Cu grid (200 mesh) and dried at room temperature.

Raman spectrum of PAMPS and NPP films was obtained using a Raman spectroscopy (LabRAM Aramis, HORIBA) using a 532 nm laser. Each solution was dropcasted on a glass slide and dried at

room temperature. The area and thickness of the films were the same with the films used for thermoelectric measurement.

X-ray photoelectron spectroscopy (XPS) analysis of PAMPS and NPP65-3 films with different PVA concentration was performed using a K-alpha instrument, Thermo U. K.

Time-of-flight secondary ion mass spectrum (ToF-SIMS) analysis was performed using an ION-TOF V instrument. A 30 keV bismuth ion gun was used as a primary ion current source (0.5 pA). First, the NPP65-3 on PET film were prepared the same to the FL measurement by applying ΔT in an area of 2 × 1 cm^2 and the central part of the film cut in half (1×1 cm^2) was measured in order to confirm the distribution change of anions by thermodiffusion. Next, thermodiffusion process was examined at ΔT of 4.8 K and 80% RH for 500 s. Then, the NPP65-3 on PET film was cut into half (area of 1 × 1 cm^2). The center of the films were examined with area of 100 × 100 μm^2 for the same sputter time of 2 min. The atomic composition count was obtained by integrating each peak.

The tensile test of NPP65-3 films was performed using universal testing machine (TopTac 2000, Yeonjin Corp. Scientifics Ltd., South Korea). NPP65-3 solution was dropcasted into a rectangular Teflon mold and dried at room temperature and 40% RH during 72 h to obtain 10 mm × 30 mm rectangular shaped free-standing film with thickness of 0.3 mm. NPP65-3 films were stored in the dried (40% RH) and humid (80% RH) chamber, taken out immediately prior to measurement, and measured at 40% RH. The free-standing NPP65 films were held by pneumatic grips. The gauge length was adjusted to 20 mm and the strain rate was 0.01 mm s^{-1}.

Optical microscopy was performed by a BA310MET, Motic.

Thermogravimetric analysis (TGA) was performed using an SDT Q600, TA Instruments.

Numerical simulation was carried out using COMSOL Multiphysics. The thermoelectric voltage generation of NPP65-3 device was computed through 3D models of NPP65-3 film (thickness: 60 μm, width: 4 mm, length: 4 mm) and Au electrodes (thickness: 100 nm, width: 1 mm, length: 4 mm). The input parameters of the NPP65-3 film were the heat capacity (154.4 J kg^{-1} K^{-1}), density (1100 kg m^{-3}),

Seebeck coefficient (−25 mV K^{-1}), and thermal conductivity (0.41 W m^{-1} K^{-1}).

The thermovoltage (V_{out}) and current (I) were measured by a homemade setup with a Keithley 6514 Electrometer or a Keithley 2182A Nanovoltmeter.[20, 21] Two Peltier devices attached to an aluminum heat sink using a thermal paste (~4 mm apart) generated the temperature gradient. The temperature gradient was set by applying various input currents (+0.5 to −0.5 A), on the two Peltier devices using a Keithley 2400 Multimeter. The temperature difference in the samples was checked by using a high-resolution IR camera (FLIR E40) in a dark room at room temperature (23−26 °C with an error of 0.2 °C). The humidity during the V_{out} measurement was controlled by the volume of deionized water in the sealed chamber. The RH was measured by a hygrometer (sensitivity of 1% RH). The V_{out} of the TE device was measured after saturation of a specific humidity (1 h) and stabilization of the voltage signal. For storage stability measurement, the film was kept in a chamber at RH 50% in refrigerator, and after a specific time past, the V_{out} measurement was repeated at RH 80%, ΔT of 4.8 K, and RT condition. The I measurement was performed in the same condition. For the photothermal experiment, the NIR coherent diode laser (808 nm, 0−1.0 W, 3-Laser Technology) was exposured perpendicularly to the PEDOT:Tos electrodes (15 cm apart), and the laser beam was collimated to generate a beam area of 2 × 3.5 mm^2. The temperature gradient and time-drive temperature change of the films were measured using the IR camera and control programmed software in a thermally stabilized dark room at room temperature, which was set to 23−25 °C with an error of 0.2 °C, for clear analysis.

The electrochemical impedance spectroscopy (EIS) was performed using an electrochemical interface and impedance analyzer (COMPACTSTAT, IVIUM technology). The samples (area of 5 mm × 5 mm) were measured by 2-electrode setup at room temperature and different RH levels. Normally, the EIS was measured in-plane direction through the film on substrate with Au electrodes. The EIS spectrum was fit using the equivalent circuit mode (Figure S12i) and the simulated parameters were summarized in Table S1.

To check isotropy of NPP65-3 film on PET film, the EIS was also measured out-of-plane direction

through the perpendicular direction to the film with Au electrodes, and the following ionic conductivity was 14.5±0.5 S m^{-1}, similar to the in-plane ionic conductivity (15.9±0.5 S m^{-1}), indicated the NPP65-3 film was isotropic.

The thermal conductivity (κ) was calculated from the equation $\kappa = C_p\, \alpha\, \rho$, where C_p is the specific heat capacitance, α is the thermal diffusivity, and ρ is the density of the sample. The C_p was measured from differential scanning calorimetry (DSC, 200 F3 Maia, NETZSCH) under N_2 gas flow at a heating rate of 10 °C min^{-1}. The in-plane α was measured by laser flash analysis (LFA457, NETZCH) at a 25 °C chamber and 40% RH. NPP composite solution was dropcasted into a rectangular shaped Teflon mold and dried at room temperature for 72 h to obtain a thickness of 0.5 mm. To calculate density of films (ρ_{film}) at various humidity levels (50−90% RH), the mass of the films at different RH level was measured. According to the Equation S7, the volume change by water absorption is originated from different swelling efficiency of hydrogel network with respect to the change of RH level. V_{film} and m_{film} are the volume and mass of the film measured at 40% RH as an initial value.[16, 22] V_{total} is calculated as the product of area and thickness of the film.

$$V_{total}(RH) = V_{film}(RH) + V_{water}(RH)$$
$$= m_{film}(RH)/\rho_{film}(RH) + \Delta m_{water}/\rho_{water} \quad \text{Equation (S7)}$$

$$\rho_{film}(RH) = \frac{m_{film}(RH)}{V_{total}(RH) - \Delta m_{water}/\rho_{water}} \quad \text{Equation (S8)}$$

The weight of the samples at different RH level was measured for the sample stored in the chamber of corresponding humidity prior to use. Δm_{water} was calculated from the change in mass of the film between a particular RH level and 40% RH. The water density (ρ_{water}) of 0.997 g cm^{-3} was used for the calculation. Therefore, the ρ_{film}(RH) was calculated from Equation S8.

The κ of the NPP samples at various humidity levels (50−90% RH) was calculated from the Equation S9.

$$\kappa = \kappa_p \emptyset_p + \kappa_w \emptyset_w \quad \text{Equation (S9)}$$

where ø is volume fraction. The subscripts p and w corresponded to the NPP sample at 40% RH and water, respectively. The κ_w of 0.6 W m^{-1} K^{-1} was used for the calculation.

The electrochemical energy storage E_{ch} was calculated from the Equation S10.[23]

$$E_{ch} = \frac{1}{2}C(S_i\Delta T)^2 \qquad \text{Equation (S10)}$$

where C is the capacitor (in here 1 mF), S_i is the ionic Seebeck coefficient, and ΔT is the temperature gradient across the two electrodes (in here 5 K).

Energy density (E, J m^{-2}) and power density (P, W m^{-2}) of the band-type TE module was calculated from the Equation S11–S12.

$$E = \frac{E_{ch}}{A} \qquad \text{Equation (S11)}$$

$$P = \frac{V_{out}I}{A} \qquad \text{Equation (S12)}$$

where E_{ch} is the electrochemical energy storage calculated using the capacitor (in here 1 mF) and the ΔT (in here 3.7 K), A is the total area of the legs of the module, V_{out} is the thermovoltage, and I is the current.

The maximum charging efficiency of ionic thermoelectric supercapacitor (η_{iTE}) was calculated from the Equation S13.[23]

$$\eta_{iTE} = \frac{\Delta T}{T_H} \frac{ZT_i}{2ZT_i + \frac{10T}{T_H} - \frac{1}{2}ZT_i\frac{\Delta T}{T_H}} \qquad \text{Equation (S13)}$$

where T_H is the temperature at hot part, ZT_i is the ionic figure of merit, and T is the absolute temperature on thermoelectric measurement. The η_{iTE} for organic ionic thermoelectric materials in Table 1 and Figure S17 was determined from Equation S13.

The maximum thermoelectric efficiency (η_{max}) of conventional thermoelectric materials was calculated from the Equation S14.

$$\eta_{max} = \frac{\Delta T \sqrt{1+ZT} - 1}{T_H \sqrt{1+ZT} + \frac{T_C}{T_H}}$$

Equation (S14)

where T_C is the temperature at cold part and ZT is the figure of merit. The η_{max} for inorganic thermoelectric materials in Table 1 and Figure S17 was determined from Equation S14.

The ion transport rate (J_i) was calculated from the Equation S15.[24]

$$J_i = \frac{I_{sc}}{z_i F}$$

Equation (S15)

where I_{sc} is the short-circuit current, z_i is the ion valence and F is the Faraday constant.

2. Supplementary Tables

Table S1. Summary of simulated impedance parameters obtained by fitting the electrochemical impedance spectroscopy results.

Sample	RH (%)	C_{geo}[a] (F)	L[b] (μH)	Z_i[c] (Ohm)	Z_e[d] (Ohm)
NPP33-3	80	3.02E-11	66.3	753	3.57E+06
NPP52-3	80	2.93E-11	55.0	647	1.46E+06
NPP65-1	80	2.26E-11	76.7	921	1.43E+06
NPP65-2	80	2.48E-11	57.5	690	3.67E+06
NPP65-3	50	1.83E-11	306.9	3013	1.61E+06
	60	2.00E-11	119.5	1346	1.52E+06
	70	2.11E-11	87.6	1099	3.57E+06
	80	3.02E-11	54.5	632	1.23E+06
	90	4.04E-11	41.0	435	1.53E+06
NPP65-4	80	9.60E-12	42.6	540	3.43E+06
NPP65-5	80	2.87E-11	46.2	525	3.01E+06
NPP78-3	80	2.95E-11	52.1	607	1.15E+06
NPP97-3	80	2.83E-11	50.7	599	1.05E+06
NPP130-3	80	2.52E-11	44.4	527	3.50E+06
NPP65-3-PVA 0 wt%	80	3.07E-11	50.8	586	2.21E+06
NPP65-3-PVA 9 wt%	80	2.89E-11	54.5	751	1.85E+06
NPP65-3-PVA 16 wt%	80	2.56E-11	61.1	921	3.19E+06
PAMPS	80	2.61E-11	76.7	1057	-

[a] Geometrical capacitance. [b] Inductance. [c] Ionic and [d] electronic impedance calculated for the films from the simulated electrochemical impedance spectrum in Figure S12. The film samples contained 2 wt% PVA unless indicated otherwise.

Table S2. Summary of thermoelectric parameters for NPP films.

Sample	RH (%)	t^a (μm)	$\sigma_i{}^b$ (S m^{-1})	$\sigma_e{}^c$ (mS m^{-1})	$S_i{}^d$ (mV K^{-1})	$PF_i{}^e$ (mW m^{-1} K^{-2})	κ^f (W m^{-1} K^{-1})	$ZT_i{}^g$
NPP65-3	50	40±2	4.98±0.83	9.32±2.89	-16.1±0.8	1.30±0.18	0.35±0.03	1.1±0.3
	60	43±2	10.4±0.8	9.21±3.03	-18.6±1.0	3.62±0.33	0.36±0.03	3.0±0.6
	70	46±2	11.9±0.5	3.67±2.05	-22.0±1.1	5.76±0.44	0.38±0.04	4.6±0.7
	80	60±3	15.9±0.5	8.18±3.33	-25.0±1.3	9.93±0.69	0.41±0.04	7.2±1.0
	90	69±3	20.0±0.5	5.68±1.86	-26.0±1.4	13.6±0.88	0.44±0.04	9.1±1.2
NPP33-3	80	60±3	13.3±0.5	2.80±1.57	-12.1±0.6	1.94±0.14		
NPP52-3	80	60±3	15.4±0.7	6.84±2.34	-15.6±0.8	3.77±0.29		
NPP78-3	80	60±3	16.5±0.8	8.68±3.77	-23.2±1.2	8.88±0.70		
NPP97-3	80	60±3	16.7±0.8	9.51±4.52	-22.9±1.2	8.77±0.69		
NPP130-3	80	60±3	19.0±0.8	2.86±1.63	-17.3±0.9	5.67±0.44		
PAMPS	80	60±3	9.5±0.5	-	26.5±4.4	6.6±1.8		

[a] Film thickness. [b] Ionic conductivity. [c] Electrical conductivity. [d] Ionic Seebeck coefficient. [e] Ionic power factor. [f] Thermal conductivity. [g] Ionic figure of merit.

Table S3. Summary of thermoelectric parameters of the NPP film and other organic or inorganic thermoelectric materials reported in the literature.

Sample	Major[a] carrier, type	T[b]	ΔT[c]	σ_i[d] (S m^{-1})	σ_e[e] (mS m^{-1})	S[f] (mV K^{-1})	PF[g] (mW m^{-1} K^{-2})	k[h] (W m^{-1} K^{-1})	ZT[i]	η[j] (%)	Ref.
NPP65-3	I, n		4.8	15.9	8.18×10^{-3}	−25.5	10.3	0.41	7.5	0.48	This work
NPC40	I, n	298	4.5	5.26	0.3	−18.2	1.74	0.34	1.53	0.18	[21]
HDH30	I, p	298	5	29.1	30	16.2	7.64	0.50	4.51	0.40	[25]
PEDOT-Tos/SWCNT+TDAE	I, p	300	20	6.4		14	1.25	0.52	0.72	0.42	[26]
EMIM-DCA/PVDF-HFP	I, p	298	0.6	0.67		26.1	0.455	0.175	0.75	0.015	[27]
PSSNa	I, p	298	8	1.18		4	0.02	0.49	0.012	0.0032	[23]
PEDOT:PSS	I, p	298	1	0.08		2.6	0.00054	0.3	0.00054	0.0001	[28]
EMIM:DCA/SWNT/SDS	I, p	296	0.5	0.094	0.000006	23	0.05	0.273	0.054	0.00090	[29]
GO	E, p	295	10.5	0.03		9	0.00243				[30]
PSSH (PANI-Gr-CNT)	I, p	295		9		8	0.58	0.38	0.4		[31]
$Na_{0.03}Sn_{0.992}Se$	E, p	783	10[k]		11800	0.27	0.86	0.21	3.1	0.43	[32]
		300	10[k]		8500	0.19	0.29	0.65	0.13	0.10	
$Bi_{0.48}Sb_{1.52}Te_3$	E, p	330	10[k]		55000	0.246	3.3	0.75	1.3	0.67	[33]
		300	10[k]		63700	0.236	3.5	0.80	1.4	0.68	
$Pb_{0.98}Na_{0.02}Te$–SrTe 8%	E, p	923	10[k]		30000	0.295	2.61	1	2.4	0.32	[34]
		300	10[k]		209000	0.089	1.66	2.9	0.17	0.13	
$PbTe_{0.7}S_{0.3}$ - 2.5% K-doped	E, p	923	10[k]		16000	0.298	1.42	0.6	2.2	0.30	[35]
		300	10[k]		146000	0.071	0.74	1.56	0.14	0.11	
SnSe (b axis)	E, p	923	10[k]		9000	0.33	0.98	0.35	2.6	0.33	[36]
		300	10[k]		1100	0.50	0.28	0.71	0.12	0.09	
$Cu_{1.94}Al_{0.02}Se$	E, p	1029	10[k]		27500	0.249	1.7	0.67	2.6	0.30	[37]
		300	10[k]		170000	0.078	1.0	1.2	0.26	0.19	
$(Cu_{0.78}Ag_{0.22})_2(Te_{0.78}S_{0.22})$	E, p	1000	10[k]		20000	0.225	1.0	0.52	2.0	0.26	[38]
		300	10[k]		46100	0.068	0.21	0.40	0.16	0.16	
Te-PEDOT:PSS NW	E, p	400	6		7230	0.325	0.76	0.59	0.54	0.16	[39]
		300	6		4310	0.311	0.42	0.68	0.18	0.08	
$Bi_2Te_{2.79}Se_{0.21}$ + 0.067 wt% $BiCl_3$	E, n	350	10[k]		99200	−0.21	4.4	1.1	1.4	0.61	[40]
		300	10[k]		121300	−0.20	4.8	1.11	1.3	0.66	
$Bi_2Te_{2.79}Se_{0.21}$	E, n	357	10[k]		94000	−0.197	3.6	1.1	1.2	0.54	[41]
		300	10[k]		119000	−0.186	4.1	1.12	1.1	0.62	

[a] Major carrier, where I represents ionic and E represents electronic. [b] Absolute temperature. [c] Temperature gradient. [d] Ionic conductivity. [e] Electrical conductivity. [f] Seebeck coefficient. [g] Power

factor. [h] Thermal conductivity. [i] Figure of merit. [j] TE efficiency: maximum charging efficiency of iTE (η_{iTE}) for organic materials and maximum TE efficiency (η_{max}) for inorganic materials. [k] A ΔT of 10 K was set for a low temperature gradient.

3. Supplementary Figures

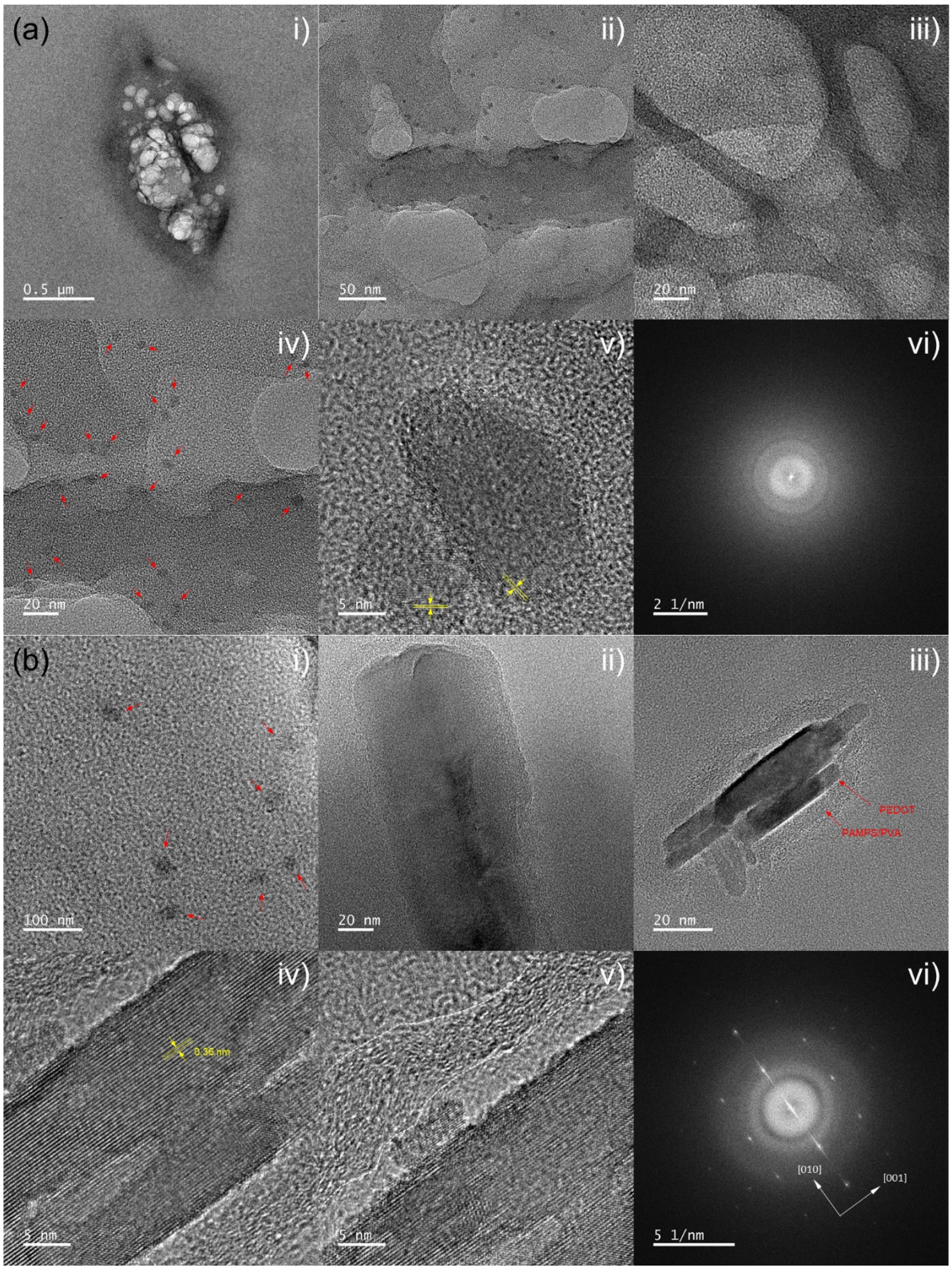

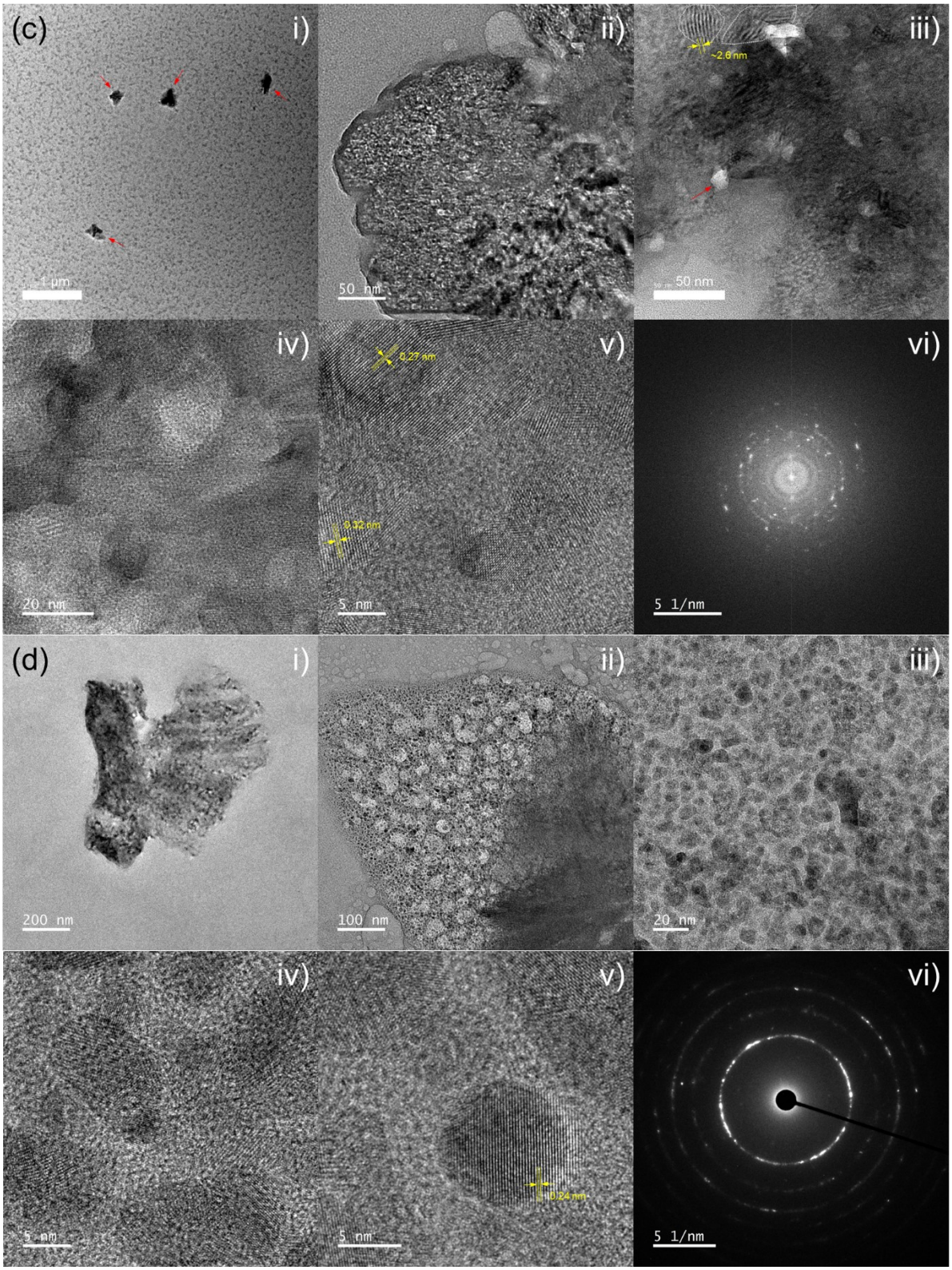

Figure S1. TEM images obtained at various magnifications. (a) PAMPS/PVA film. a-iv) The arrows indicate the nanocrystallite. a-vi) The fast Fourier transform (FFT) pattern was obtained from a-iii). (b) NPP33-3 film. b-i) The arrows indicate the single-crystal PEDOT. b-vi) The FFT pattern was obtained from b-iii). (c) NPP65-3 film. c-i) The arrows indicate the agglomerate contained PEDOT crystals in a cluster form. c-vi) The FFT pattern was obtained from c-iv). (d) NPP130-3 film. d-vi) The

electron diffraction pattern was obtained from d-iii).

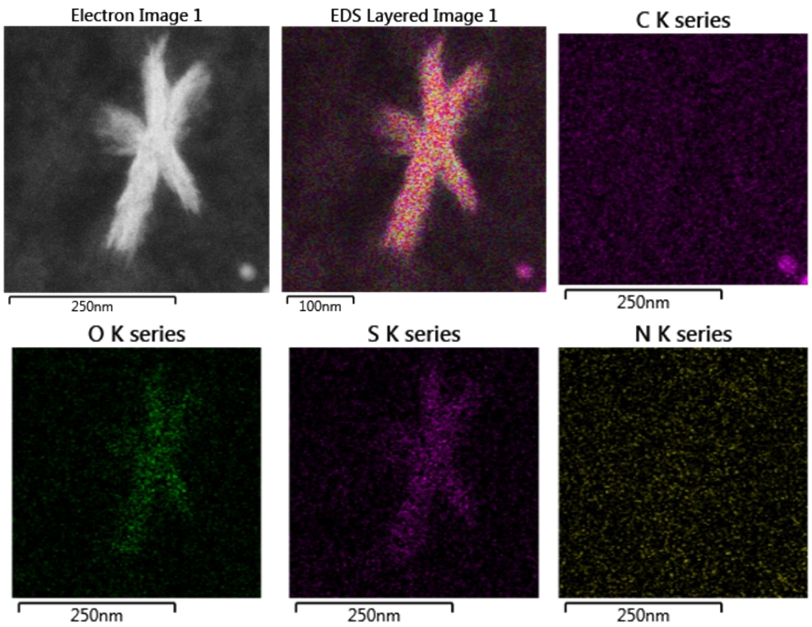

Figure S2. EDS image of the NPP65-3 film.

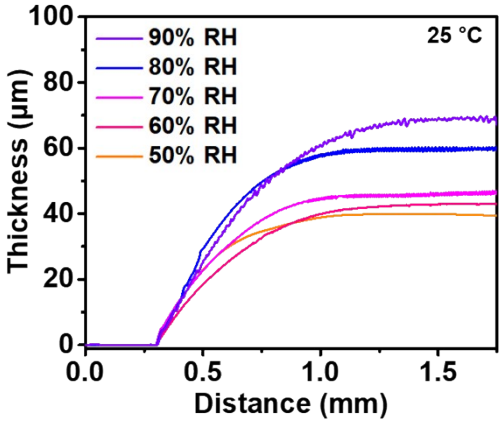

Figure S3. Thickness profile of the NPP65-3 film measured using a surface profiler at various RH levels. Samples were stored in the corresponding RH chamber and taken out immediately prior to measurement, which took 30 s.

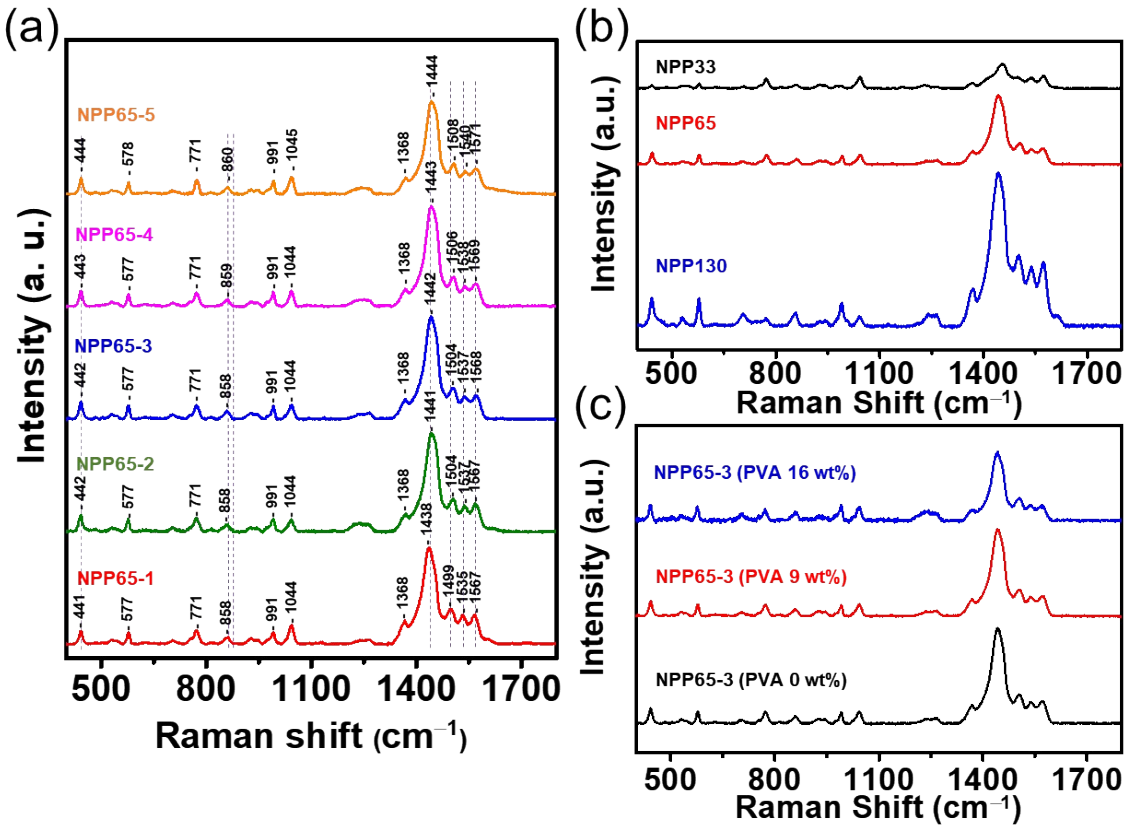

Figure S4. (a) Raman spectrum of NPP65 with different APS concentrations: (b) NPP33-3, NPP65-3, and NPP130-3 and (c) NPP65-3 with different PVA concentrations. Laser line: 532 nm.

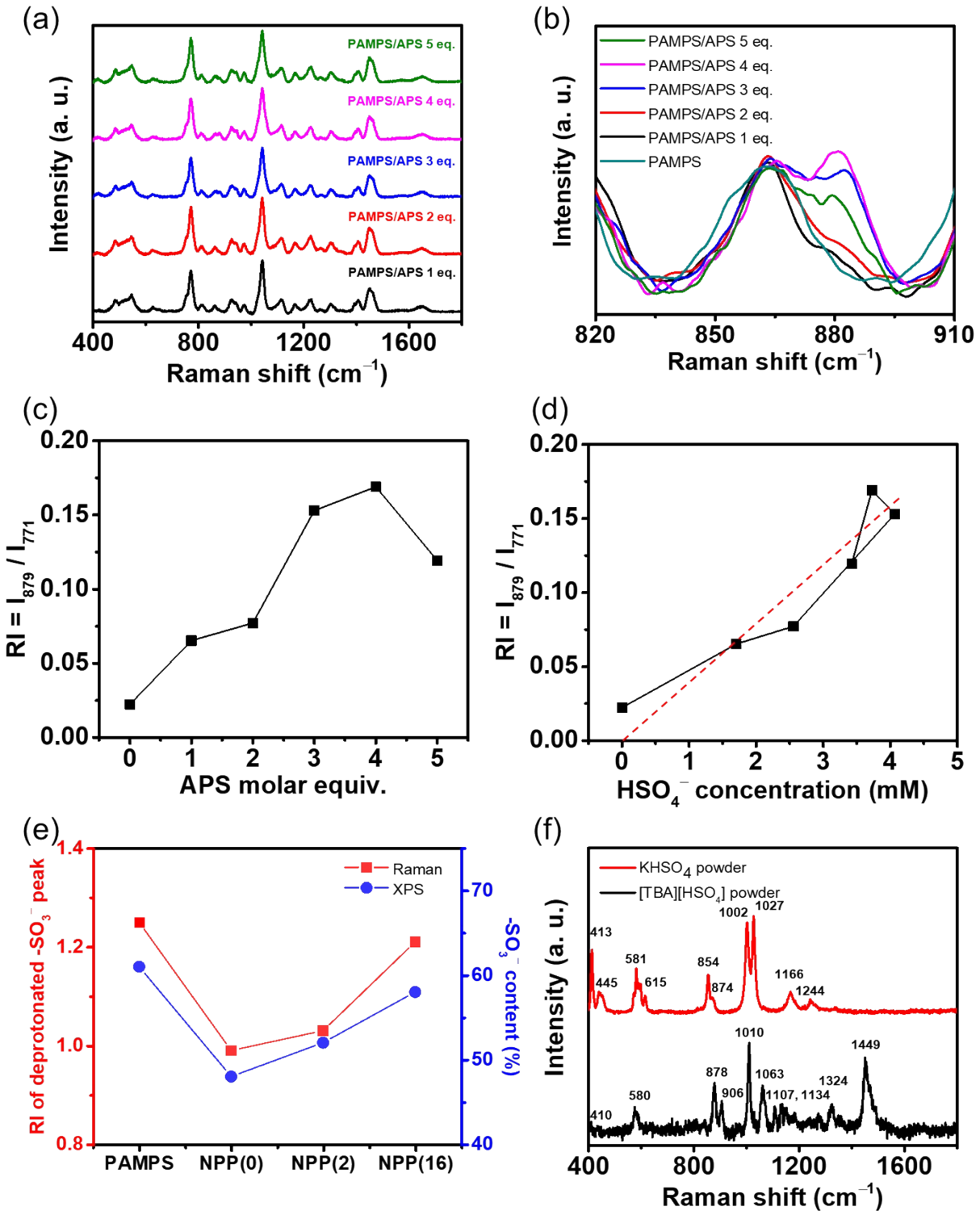

Figure S5. (a) Raman spectrum of PAMPS films with different APS contents. Relative intensity (RI) of the peak at 879 cm^{-1} versus (c) APS concentration and (d) HSO_4^- concentration obtained from FL analysis. (e) Relative intensity (RI) of the deprotonated -SO_3^- peak (Raman analysis) and the -SO_3^- contribution (XPS analysis) of PAMPS and NPP65-3 with different PVA contents (wt%). At PVA(*x*), *x* indicates the PVA content in wt% in the NPP65-3 film. (f) Raman spectrum of APS and $KHSO_4$ powder.

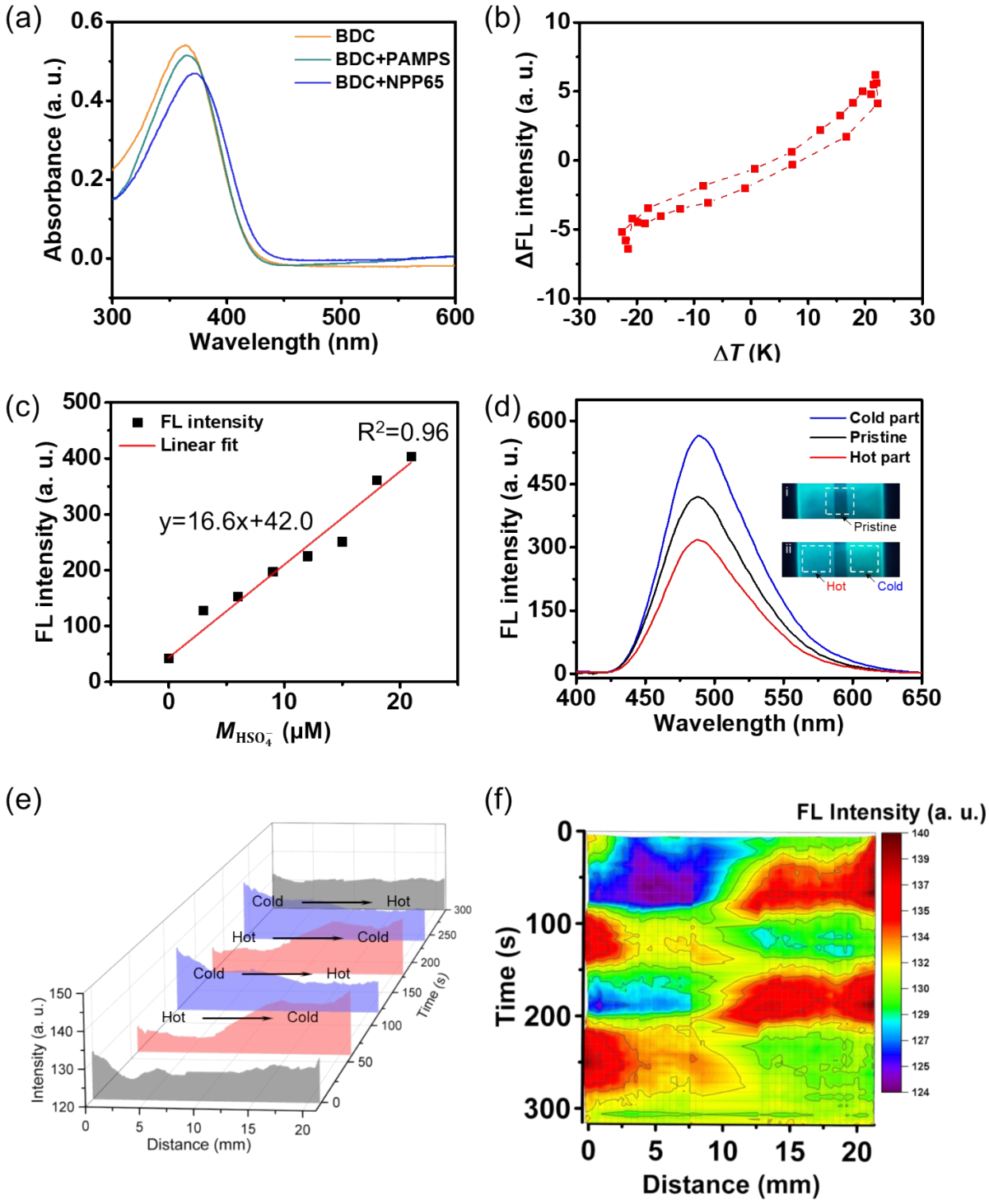

Figure S6. (a) Absorption spectrum of BDC solution (10 μM) and BDC solution upon the addition of NPP65 solution in CH_3CN:H_2O (1:1 v/v) solvent. V_{NPP65}/V_{BDC} = 1/80. (b) Difference in FL intensity between the hot and cold parts in Figure 2h at different values of ΔT during one heating–cooling cycle. (c) Linear fit of the FL titration intensity in Figure 2d. (d) FL spectrum of the NPP65-3 film with BDC for the hot and cold parts and in the pristine state, prepared at a ΔT of 4.8 K and 80% RH. Excitation wavelength: 370 nm. Inset: Photographs taken under a UV lamp (~365 nm) by applying heating–

cooling Δ*T* cycles. (e) Corresponding fluorescence intensity profile over time of Figure 2e.

To confirm the diffusion of the bisulfate anion in the film, the NPP65 films were prepared on glass slides (area=1×2 cm^2) by drop-casting 240 μL of NPP65-3 solutions and drying for 3 h at room temperature. Subsequently, a temperature gradient (Δ*T*) of 4.8 K was applied on both ends of the film at 80% RH. After an interval of 500 s to allow for sufficient diffusion of the ions and molecules, both ends of the films were cut to a size of 1×1 cm^2 and redissolved in 4 mL of deionized water. Figure S6d shows the FL spectrum of the BDC solutions mixed with the redissolved NPP65-3 film. The thermodiffusion of the bisulfate anion was confirmed by comparing the FL intensity of the two BDC solutions mixed with the cold and hot parts of the film. The FL intensity for the cold part was 1.8 times higher than that for the hot part, indicating that bisulfate anions migrated from the hot to cold parts. In addition, the FL intensity for the pristine state without an applied Δ*T* was 1.3 times higher than that of the hot part. This phenomenon of reversible FL intensity switching on the film can be clearly observed in the photographs (Figure S6d, inset).

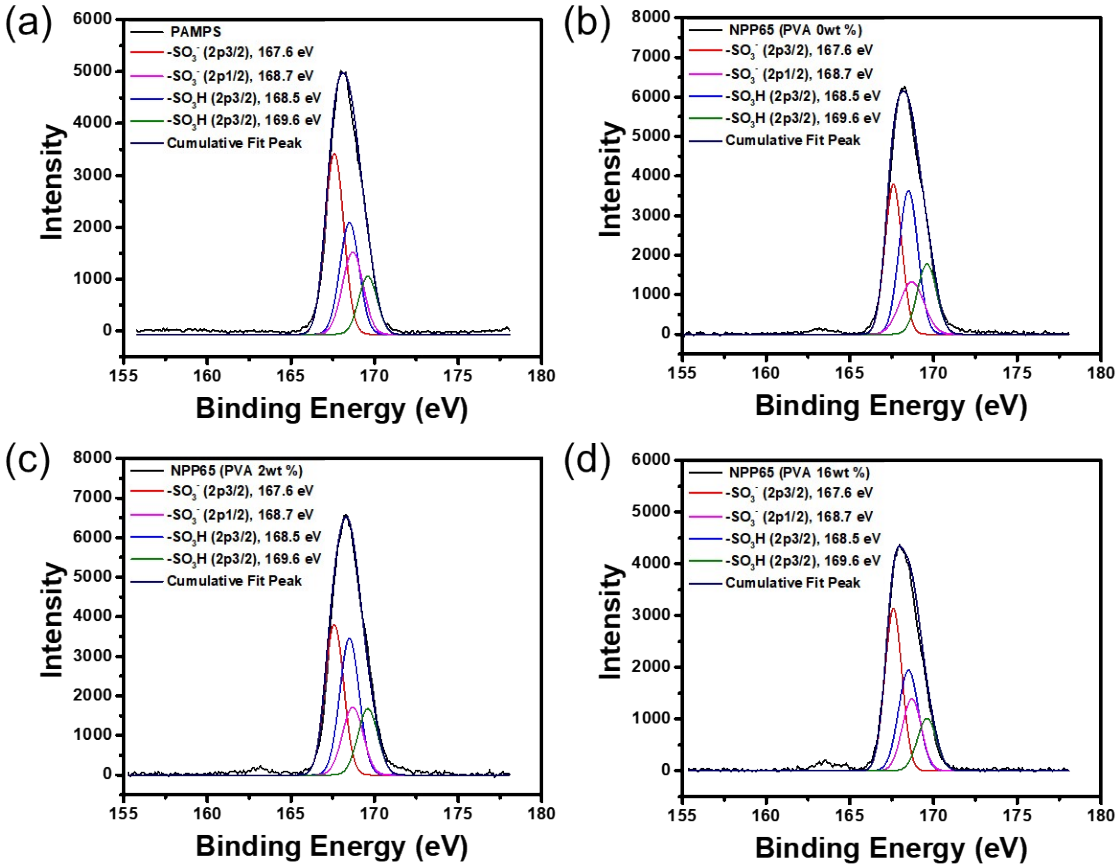

Figure S7. XPS spectra of (a) PAMPS and (b–d) NPP65-3 with different PVA contents including deconvoluted S 2p peaks.

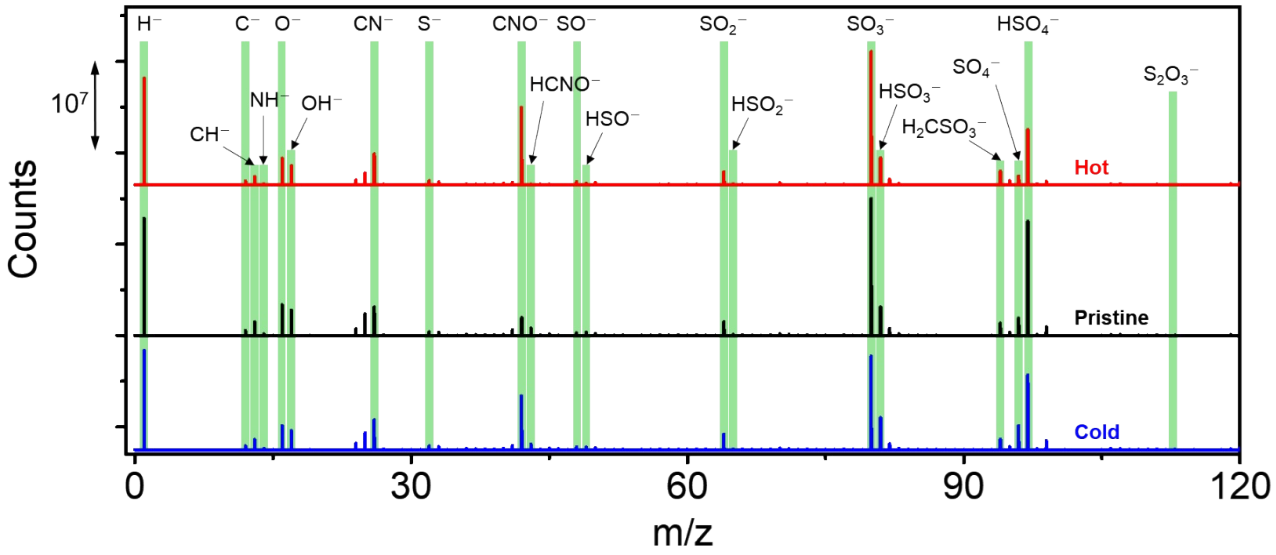

Figure S8. ToF-SIMS in the negative ion mode of the surfaces of cut NPP65 films after ion carrier transfer by applying a ΔT of 4.8 K and 80% RH.

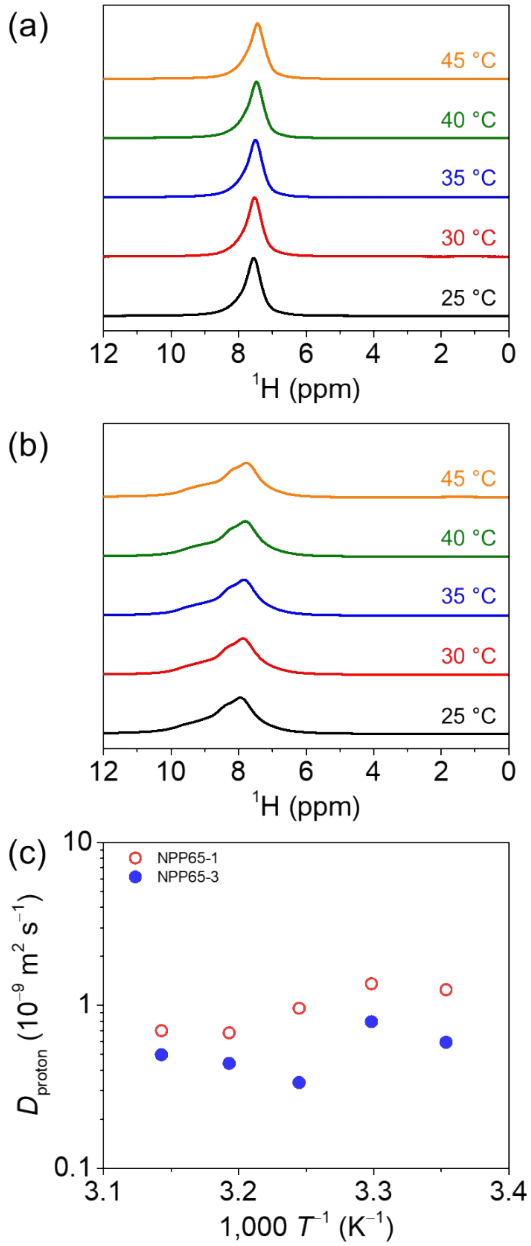

Figure S9. Solid-state ^{1}H NMR spectrum of (a) NPP65-1 and (b) NPP65-3 at 90% RH and various temperatures. (c) Diffusion coefficient of protons determined from (a,b) using the Stejskal−Tanner equation (Equation S1)

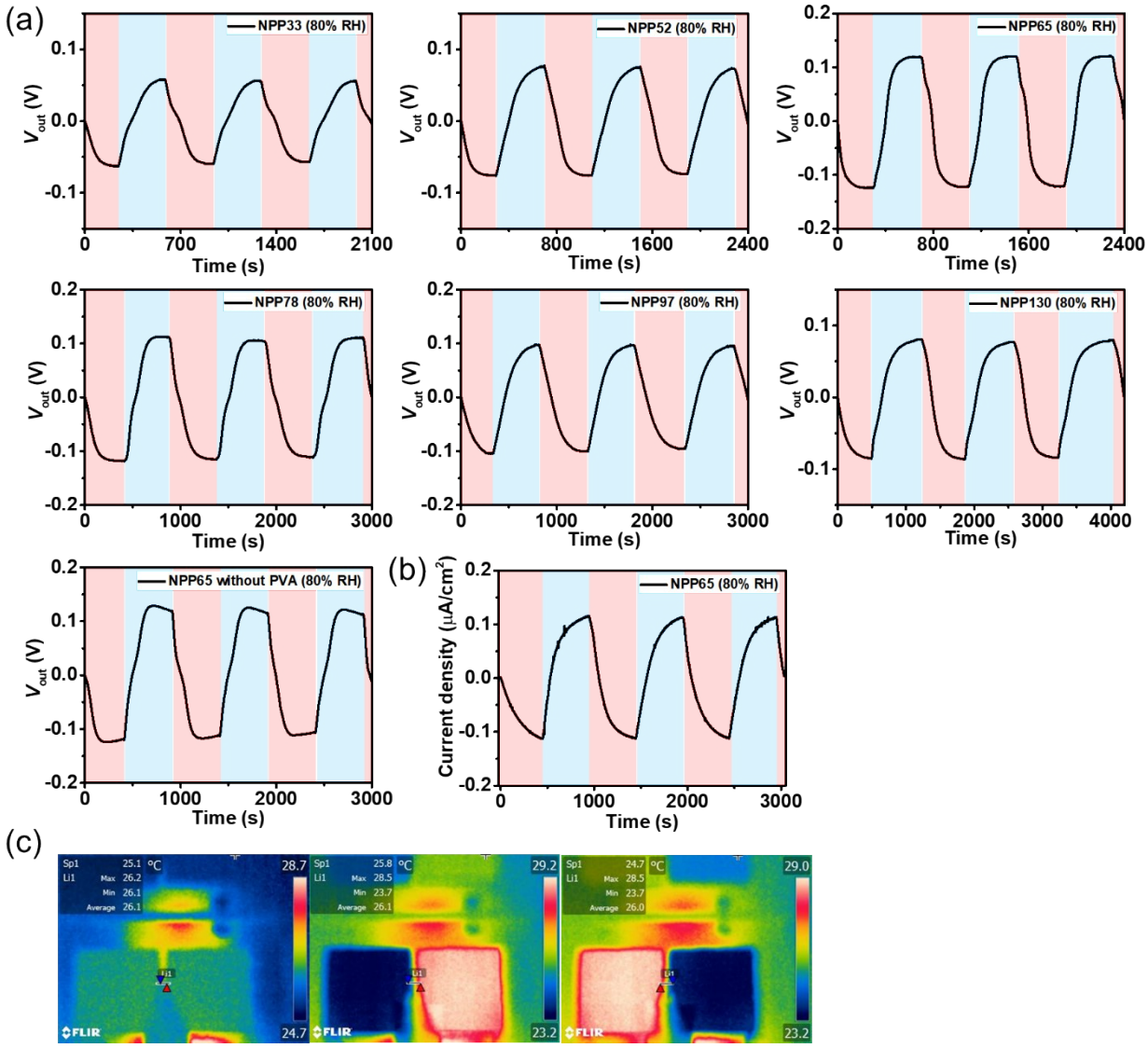

Figure S10. (a) Output voltage of NPP-3 films and NPP65-3 without a PVA film under 3 repeated heating–cooling cycles at a ΔT of 4.8 K and 80% RH. (b) Current profile of the NPP65-3 film under 3 repeated heating–cooling cycles at a ΔT of 4.8 K and 80% RH. (c) Thermal images of the NPP65-3 film placed in the middle of two Peltier devices with a gap of 4 mm. Peltier device size: 3 × 3 cm^2.

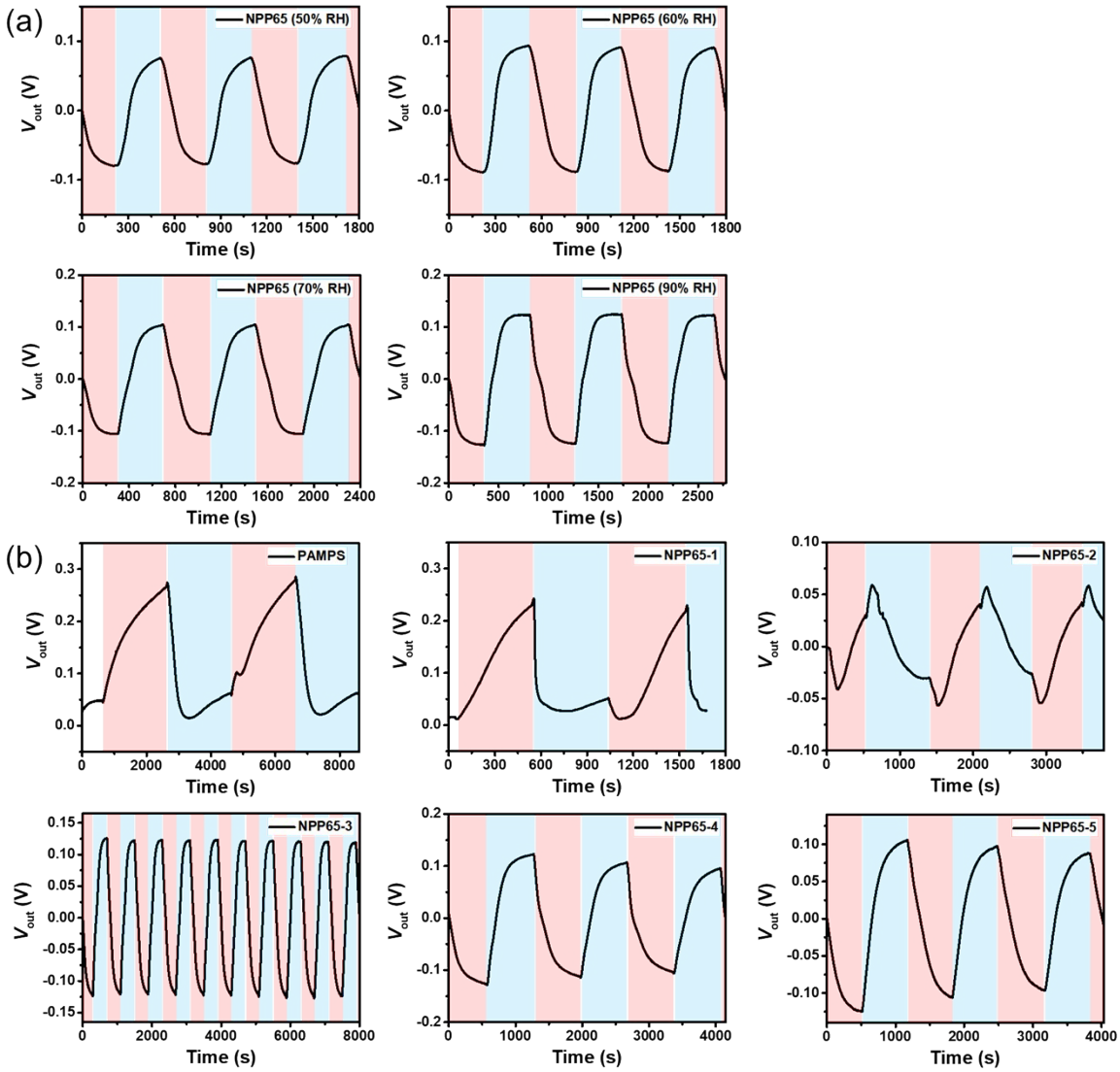

Figure S11. (a) Output voltage of NPP65-3 films under 3 repeated heating–cooling cycles at a ΔT of 4.8 K and various RH levels. (b) Output voltage of the PAMPS film and NPP65 films with various APS contents under repeated heating–cooling cycles at a ΔT of 4.8 K and 80% RH.

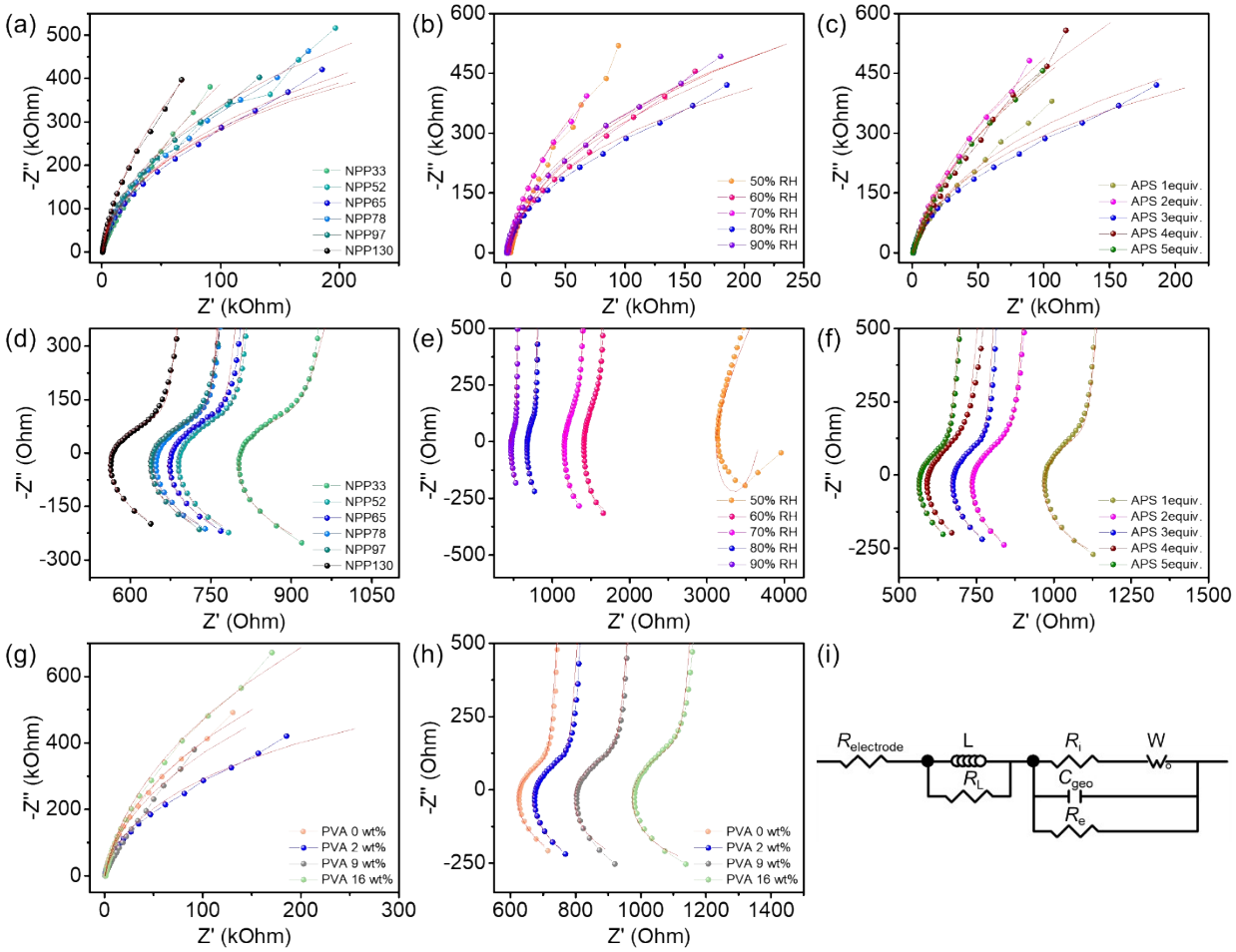

Figure S12. Nyquist plot of (a,d) NPP-3 films with various EDOT contents, (b,e) NPP65-3 films with various RH levels, (c,f) NPP65-*x* films with various APS contents, and (g,h) NPP65-3 films with various PVA contents. (i) The equivalent circuit model for obtaining each element in Table S1. The EIS was measured at an alternating voltage of 0.1 V under frequencies ranging from 1 MHz to 1 Hz. The fit line for all spectra is presented as a red line in the Nyquist plot.

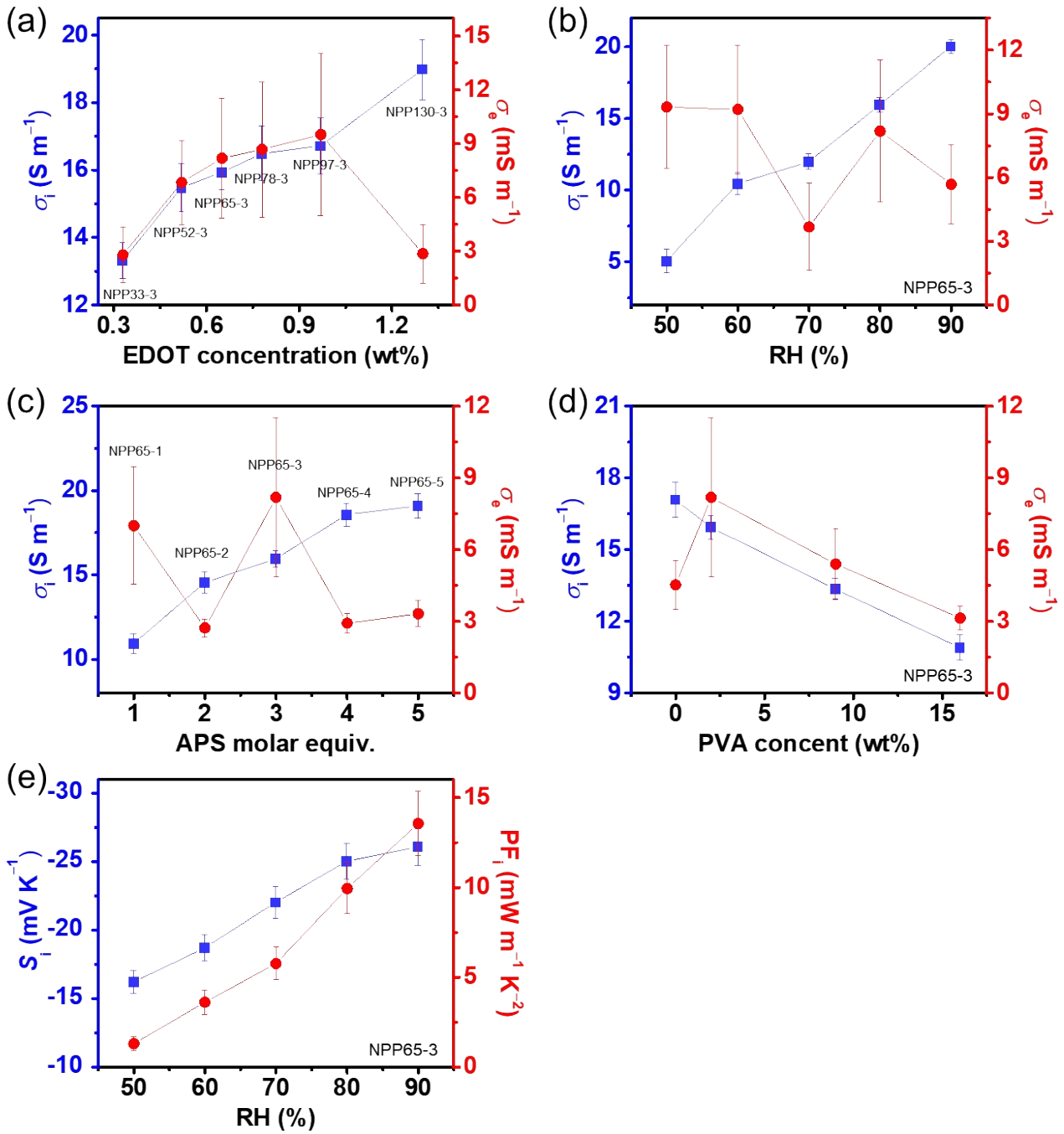

Figure S13. Ionic and electrical conductivities of (a) NPP-3 films with different EDOT concentrations, (b) the NPP65-3 film at various RH levels, (c) NPP65-*x* films with different APS contents, and (d) NPP65 films with different PVA contents. The humidity level was chosen as 80% RH for all cases. (e) S_i and PF_i of NPP films at different RH levels.

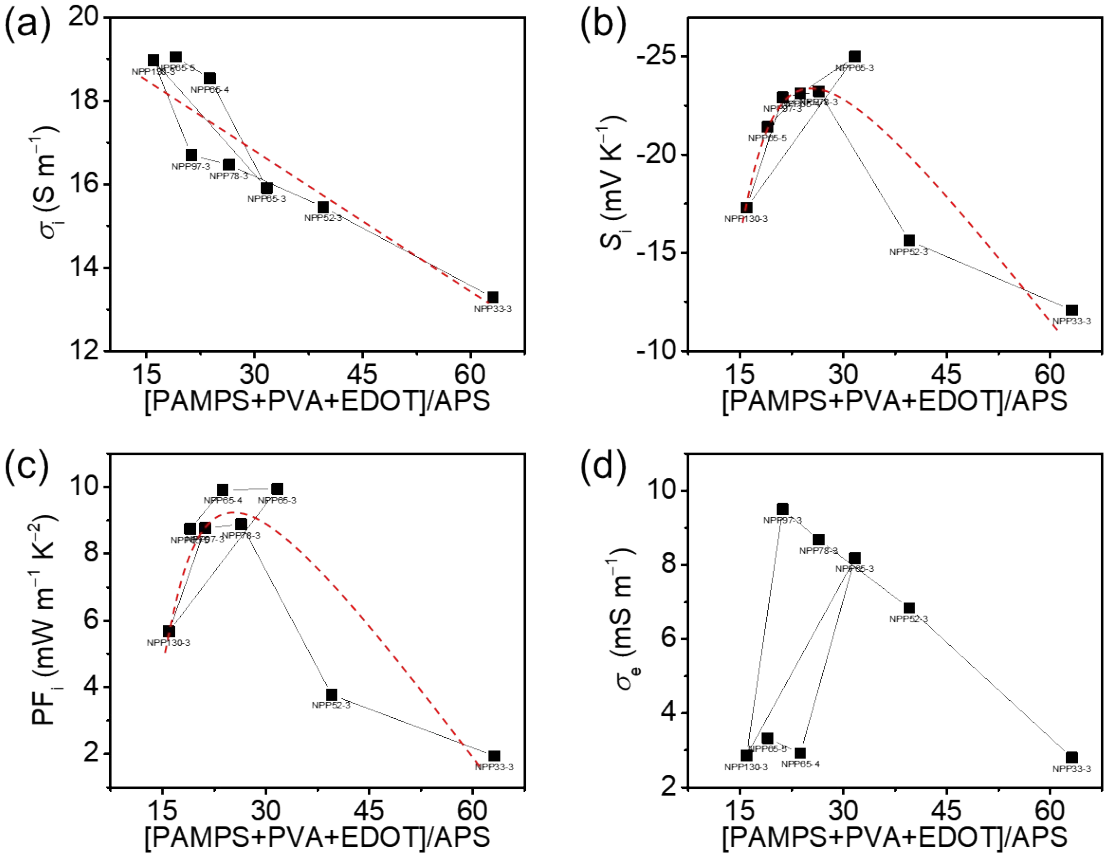

Figure S14. Correlation of iTE properties to the weight ratio, (PAMPS+PVA+EDOT)/APS. The iTE properties for (a) ionic conductivity, (b) ionic Seebeck coefficient, (c) ionic power factor, and (d) electrical conductivity. The sample number is displayed at the bottom of each data point (square**)**.

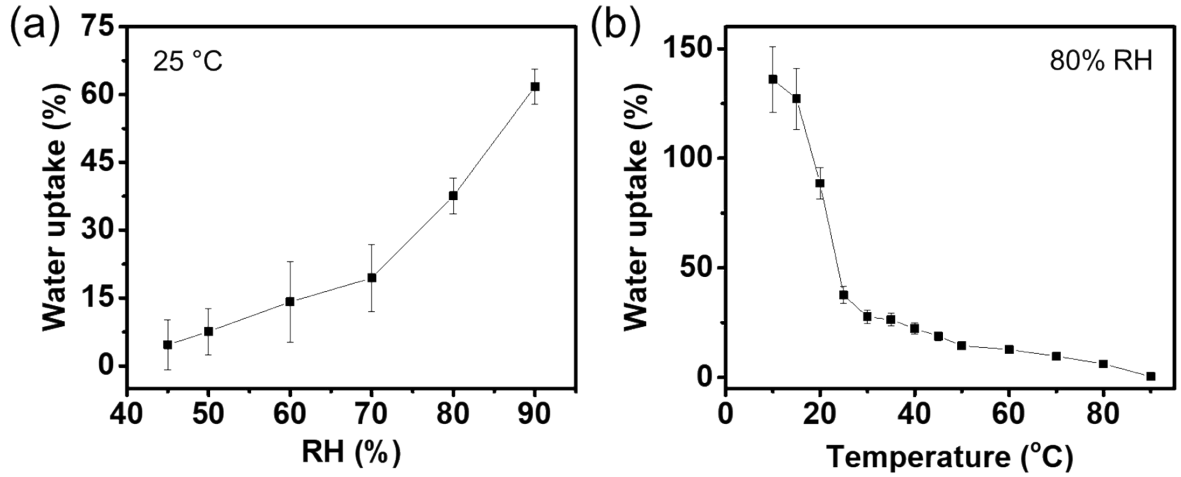

Figure S15. Water uptake ratio of the NPP65-3 film at (a) different RH levels and 25 °C and (b) different film temperatures and 80% RH.

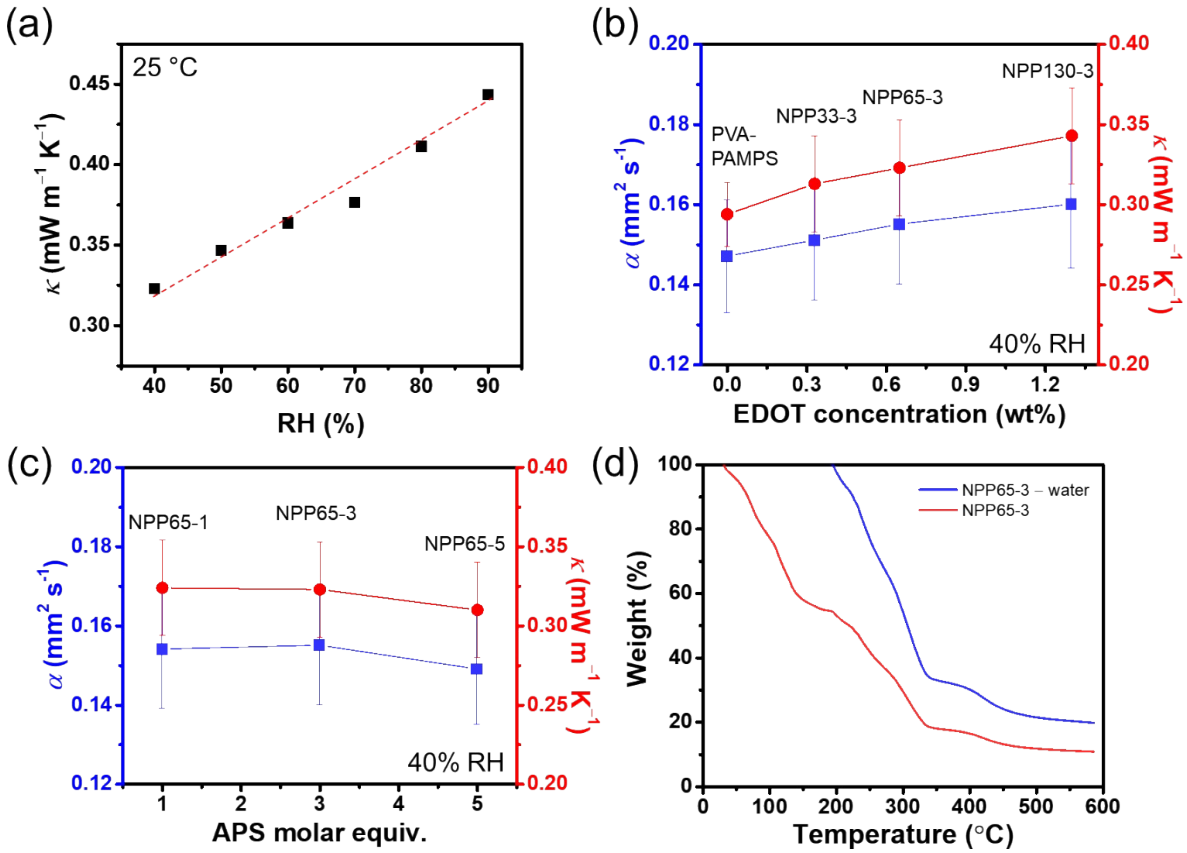

Figure S16. (a) Thermal conductivity of NPP65-3 sample at various humidity levels. Thermal diffusivity (α) and thermal conductivity (κ) of NPP samples at 40% RH with different (b) EDOT and (c) APS concentrations. The (κ) of PAMPS sample was 0.298 W m^{-1} K^{-1}. (d) Thermogravimetric analysis (TGA) curve of the NPP65-3 sample. Blue line represents the weight % after subtracting the water weight from the sample.

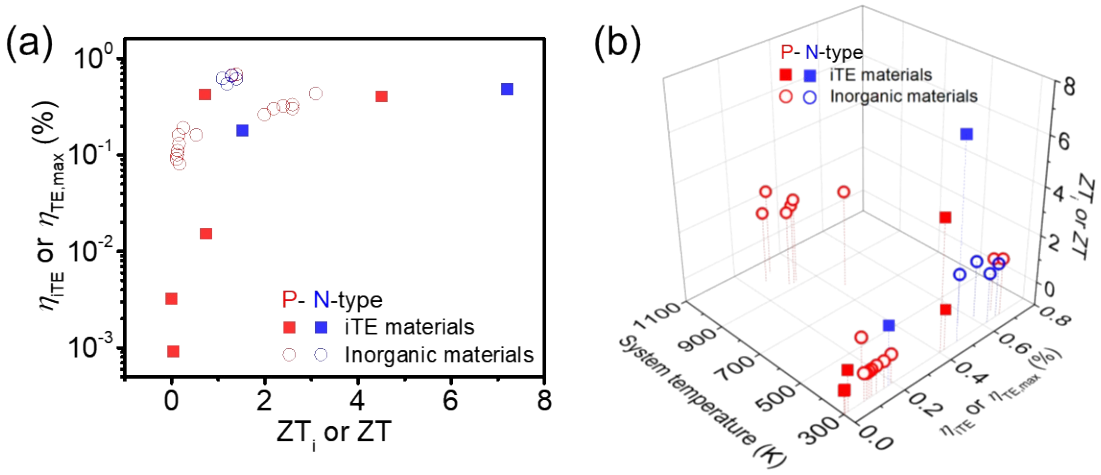

Figure S17. Comparison of the maximum thermoelectric efficiency of organic ionic thermoelectric materials and inorganic thermoelectric materials reported in the literature. The values of η_{iTE} and η_{max} were determined from Equations S13 and S14, respectively. Red and blue represent p-type and n-type materials, respectively.

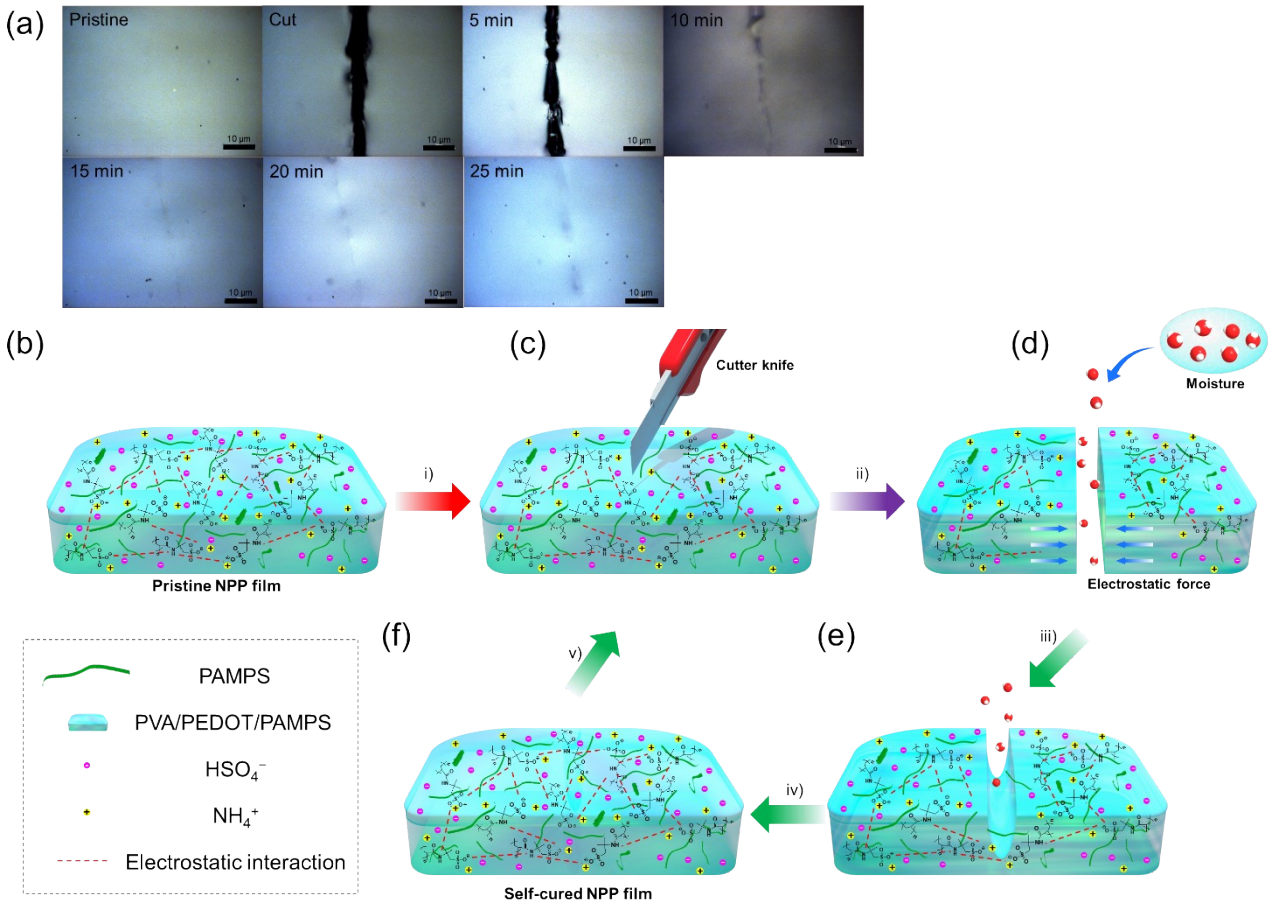

Figure S18. (a) Optical microscopy images for the self-healing test of the NPP65-3 film over time. (b–f) Schematic illustration of the intrinsic self-healing mechanism: i) the hydrogel matrix is damaged and dynamic bonds are broken by cutting, ii) moisture absorbed from air facilitates interfacial diffusion and reorganization of the hydrogel matrix at the damaged interface, iii) reversible hydrophilic bonds are recovered by electrostatic interaction over time, iv) the cut is filled and the soft film is fully cured, and v) the reversible self-healing process is possible.

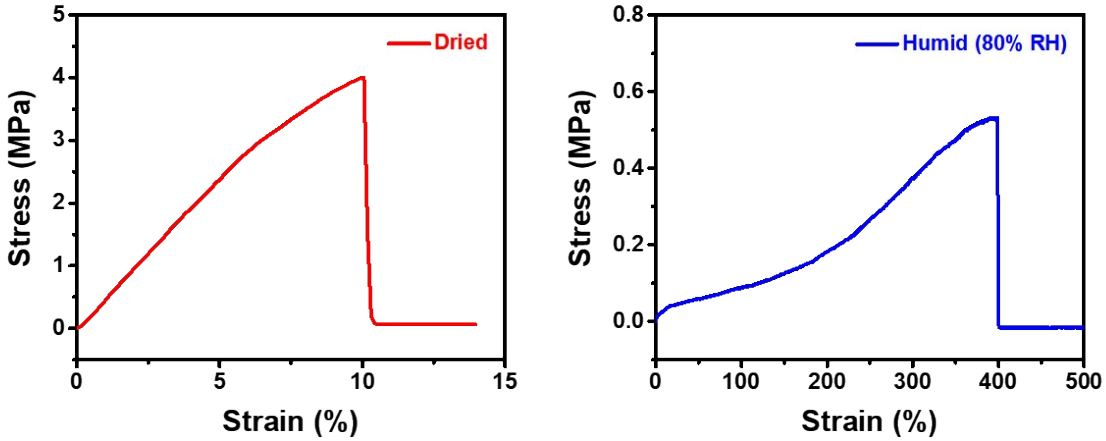

Figure S19. Stress–strain curves of the NPP65-3 film in dry (~40% RH) and humid (80% RH) states. The film was stored in the corresponding humidity chamber for 30 min and taken out immediately prior to measurement.

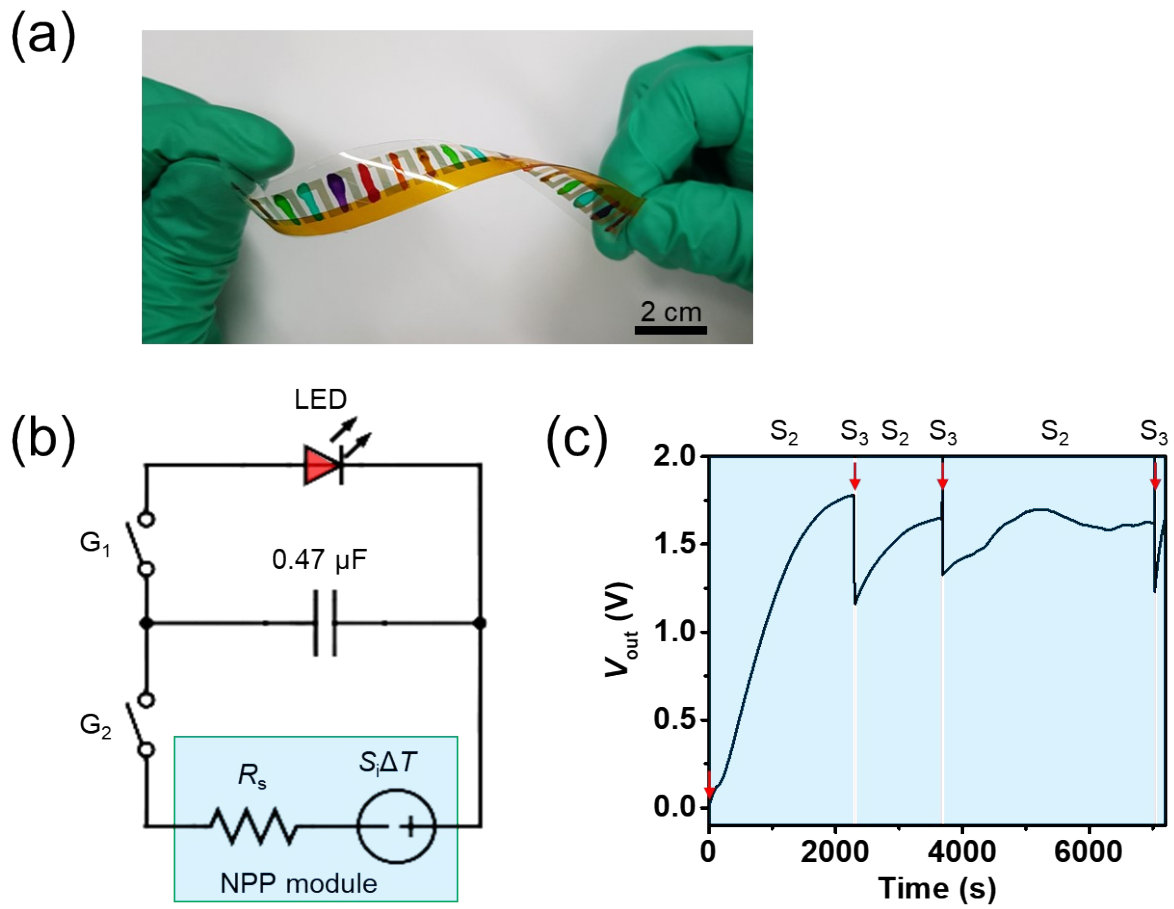

Figure S20. (a) Photograph of a flexible band-type iTE module composed of six color dyed legs prepared by drop-casted on a PET film (60 μm thick). (b) Electrical circuit used in the electrochemical energy storage and LED operation. (c) The reversible voltage switching during three repeated on/off cycles over time using the electrical circuit in (b).

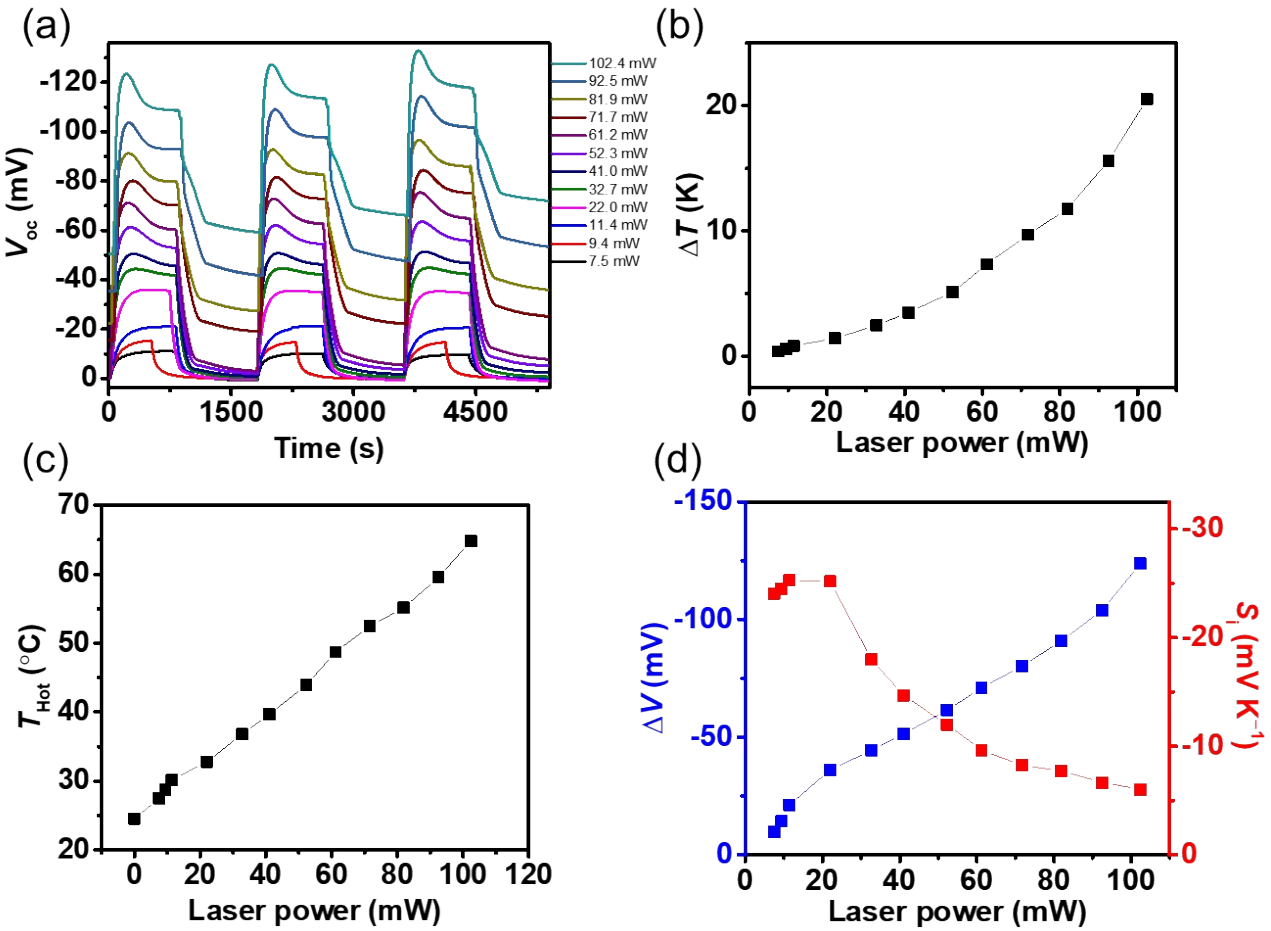

Figure S21. (a) Output voltage of NPP65-3 films under 3 repeated on–off cycles at various applied laser powers and 80% RH as well as the correlated (b) ΔT, (c) temperature of the hot part, (d) ΔV, and S_i.

4. Supplementary References

1. S. Bednarz, A. Błaszczyk, D. Błażejewska and D. Bogdał, *Catal. Today*, 2015, **257**, 297-304.
2. K. I. Seo and I. J. Chung, *Polymer*, 2000, **41**, 4491-4499.
3. H. J. Kim, S. Bhuniya, R. K. Mahajan, R. Puri, H. Liu, K. C. Ko, J. Y. Lee and J. S. Kim, *Chem. Commun.*, 2009, **46**, 7128-7130.
4. V. Kumar, A. Kumar, U. Diwan and K. K. Upadhyay, *Chem. Commun.*, 2012, **48**, 9540-9542.
5. E. O. Stejskal and J. E. Tanner, *J. Chem. Phys.*, 1965, **42**, 288-292.
6. I. Nicotera, T. Zhang, A. Bocarsly and S. Greenbaum, *J. Electrochem. Soc.*, 2007, **154**, B466.
7. G. Ye, N. Janzen and G. R. Goward, *Macromolecules*, 2006, **39**, 3283-3290.
8. B. Mattsson, A. Brodin, L. M. Torell, H. Rinne, J. Hamara, F. Sundholm and P. Jacobsson, *Solid State Ion.*, 1997, **97**, 309-314.
9. C.-C. Yang, S. J. Lue and J.-Y. Shih, *J. Power Sources*, 2011, **196**, 4458-4467.
10. G. Sonmez, P. Schottland and J. R. Reynolds, *Synth. Met.*, 2005, **155**, 130-137.
11. Q. Wu, J. Wei, B. Xu, X. Liu, H. Wang, W. Wang, Q. Wang and W. Liu, *Sci. Rep.*, 2017, **7**, 41566.
12. B. Kim, M. Han and E. Kim, *J. Mater. Chem. A*, 2019, **7**, 2066-2074.
13. S. R. S. Kumar, N. Kurra and H. N. Alshareef, *J. Mater. Chem. C*, 2016, **4**, 215-221.
14. S. H. Lee, H. Park, S. Kim, W. Son, I. W. Cheong and J. H. Kim, *J. Mater. Chem. A*, 2014, **2**, 7288-7294.
15. M. Reyes-Reyes, I. Cruz-Cruz and R. López-Sandoval, *J. Phys. Chem. C*, 2010, **114**, 20220-20224.
16. Z. A. Akbar, J.-W. Jeon and S.-Y. Jang, *Energy Environ. Sci.*, 2020, **13**, 2915-2923.
17. J.-W. Jeon, Y. Ma, J. F. Mike, L. Shao, P. B. Balbuena and J. L. Lutkenhaus, *Phys. Chem. Chem. Phys.*, 2013, **15**, 9654-9662.
18. D. A. House, *Chem. Rev.*, 1962, **62**, 185-203.
19. S. Ahmadi, C. A. Igwegbe and S. Rahdar, *Int. J. Ind. Chem.*, 2019, **10**, 249-260.
20. T. Park, C. Park, B. Kim, H. Shin and E. Kim, *Energy Environ. Sci.*, 2013, **6**, 788-792.
21. B. Kim, J. U. Hwang and E. Kim, *Energy Environ. Sci.*, 2020, **13**, 859-867.
22. F. Jiao, A. Naderi, D. Zhao, J. Schlueter, M. Shahi, J. Sundstrom, H. Granberg, J. Edberg, U. Ail, J. Brill, T. Lindstrom, M. Berggren and X. Crispin, *J. Mater. Chem. A*, 2017, **5**, 16883-16888.
23. H. Wang, D. Zhao, Z. U. Khan, S. Puzinas, M. P. Jonsson, M. Berggren and X. Crispin, *Adv. Electron. Mater.*, 2017, **3**, 1700013.
24. V. M. Barragán, *Membranes*, 2021, **11**, 480.
25. B. Kim, J. Na, H. Lim, Y. Kim, J. Kim and E. Kim, *Adv. Funct. Mater.*, 2019, **29**, 1807549.
26. K. Choi, S. L. Kim, S.-i. Yi, J.-H. Hsu and C. Yu, *ACS Appl. Mater. Interfaces*, 2018, **10**, 23891-23899.
27. H. Cheng, X. He, Z. Fan and J. Ouyang, *Adv. Energy Mater.*, 2019, **9**, 1901085.
28. W. B. Chang, H. Fang, J. Liu, C. M. Evans, B. Russ, B. C. Popere, S. N. Patel, M. L. Chabinyc and R. A. Segalman, *ACS Macro Lett.*, 2016, **5**, 455-459.
29. H. Cheng, S. Yue, Q. Le, Q. Qian and J. Ouyang, *J. Mater. Chem. A*, 2021, **9**, 13588-13596.
30. S. L. Kim, J.-H. Hsu and C. Yu, *Nano Energy*, 2018, **48**, 582-589.
31. S. L. Kim, H. T. Lin and C. Yu, *Adv. Energy Mater.*, 2016, **6**, 1600546.

32. C. Zhou, Y. K. Lee, Y. Yu, S. Byun, Z.-Z. Luo, H. Lee, B. Ge, Y.-L. Lee, X. Chen, J. Y. Lee, O. Cojocaru-Mirédin, H. Chang, J. Im, S.-P. Cho, M. Wuttig, V. P. Dravid, M. G. Kanatzidis and I. Chung, *Nat. Mater.*, 2021, **20**, 1378-1384.
33. H. Wang, G. Luo, C. Tan, C. Xiong, Z. Guo, Y. Yin, B. Yu, Y. Xiao, H. Hu, G. Liu, X. Tan, J. G. Noudem and J. Jiang, *ACS Appl. Mater. Interfaces*, 2020, **12**, 31612-31618.
34. G. Tan, F. Shi, S. Hao, L.-D. Zhao, H. Chi, X. Zhang, C. Uher, C. Wolverton, V. P. Dravid and M. G. Kanatzidis, *Nat. Commun.*, 2016, **7**, 12167.
35. H. J. Wu, L. D. Zhao, F. S. Zheng, D. Wu, Y. L. Pei, X. Tong, M. G. Kanatzidis and J. Q. He, *Nat. Commun.*, 2014, **5**, 4515.
36. L.-D. Zhao, S.-H. Lo, Y. Zhang, H. Sun, G. Tan, C. Uher, C. Wolverton, V. P. Dravid and M. G. Kanatzidis, *Nature*, 2014, **508**, 373-377.
37. B. Zhong, Y. Zhang, W. Li, Z. Chen, J. Cui, W. Li, Y. Xie, Q. Hao and Q. He, *Appl. Phys. Lett.*, 2014, **105**, 123902.
38. K. Zhao, E. Eikeland, D. He, W. Qiu, Z. Jin, Q. Song, T.-r. Wei, P. Qiu, J. Liu, J. He, B. B. Iversen, J. He, L. Chen and X. Shi, *Joule*, 2021, **5**, 1183-1195.
39. L. Yang, M. P. Gordon, A. K. Menon, A. Bruefach, K. Haas, M. C. Scott, R. S. Prasher and J. J. Urban, *Sci. Adv.*, 2021, **7**, eabe6000.
40. C. Xiong, F. Shi, H. Wang, J. Cai, S. Zhao, X. Tan, H. Hu, G. Liu, J. G. Noudem and J. Jiang, *ACS Appl. Mater. Interfaces*, 2021, **13**, 15429-15436.
41. L. Hu, H. Wu, T. Zhu, C. Fu, J. He, P. Ying and X. Zhao, *Adv. Energy Mater.*, 2015, **5**, 1500411.